ABSTRACT

RAO, NEEL. Low-Order Computational Modeling of Propeller-Wing Aerodynamic Interaction Using Wake Vortex Decomposition and Weissinger Method. (Under the direction of Dr. Ashok Gopalarathnam).

This thesis develops and demonstrates a low-order propeller wake model that efficiently calculates axial and tangential velocities in the slipstream. An approach is adopted whereby the cylindrical vortex sheet generated by a propeller in steady potential flow is decomposed into a mesh-like structure of axisymmetric vortex rings and rectilinear longitudinal filaments. The corresponding strength of each vortex system is obtained by decomposing the total circulation strength of an equivalent helical vortex in the streamwise and azimuthal directions. The geometric arrangement of the wake vortex elements is used to construct aerodynamic influence coefficient matrices, which are linearly scaled by the vortex circulation strengths to quickly calculate the propeller-induced velocities. The developed wake model is combined with the Weissinger lifting-line method to analyze propeller-wing interactions for various configurations and operating conditions. Compared with higher-order numerical methods and experimental data, the combined model gives suitable predictions of the loading distribution and total wing loading for both conventional and distributed propulsion systems. The accuracy of the model is slightly diminished for cases where hub effects and related viscous effects are significant, although general trends in the system lift and induced drag are still effectively captured.

Low-Order Computational Modeling of Propeller-Wing Aerodynamic Interaction Using Wake Vortex Decomposition and Weissinger Method

by
Neel Rao

A thesis submitted to the Graduate Faculty of
North Carolina State University
in partial fulfillment of the
requirements for the degree of
Master of Science

Aerospace Engineering

Raleigh, North Carolina

2024

APPROVED BY:

Dr. Matthew Bryant

Dr. Kenneth Granlund

Dr. Ashok Gopalarathnam
Chair of Advisory Committee

DEDICATION

To my family, especially my parents, Rajesh and Rekha, and my brother, Arjun, for their unconditional love and support.

BIOGRAPHY

Neel Rao was born on March 11, 1997, in Raleigh, North Carolina. He grew up with a keen interest in aviation and received his Private Pilot license in 2015. He completed his undergraduate studies at North Carolina State University and graduated in 2019 with a Bachelor's degree in Aerospace Engineering. He returned to NC State in the spring of 2022 to pursue a Master's degree in Aerospace Engineering. In the fall, he joined the Applied Aerodynamics Group under the guidance of Dr. Ashok Gopalarathnam. Upon graduating, Neel will continue to work in the group towards a PhD in Aerospace Engineering.

ACKNOWLEDGEMENTS

I would like to acknowledge my research advisor, Dr. Ashok Gopalarathnam, for his academic and professional guidance throughout my graduate studies. I am grateful for the opportunities he provided me while working in his lab and appreciate the invaluable insights he offered during our countless meetings and conversations. I also thank Dr. Matthew Bryant and Dr. Kenneth Granlund for dedicating their time to serve on my committee. I extend my appreciation to all the members of the Applied Aerodynamics Group for their ongoing support and give special thanks to Ryan Welker for his assistance in preparing some of the validation data that has been used in this thesis.

TABLE OF CONTENTS

LIST OF TABLES

LIST OF FIGURES

NOMENCLATURE

α	Wing geometric angle of attack
α_{0l}	Zero-lift angle of attack
$\mathcal{R}$	Wing aspect ratio
$\hat{\boldsymbol{e}}$	Unit vector
$\boldsymbol{\theta}$	Angular orientation matrix
$\boldsymbol{F}$	Aerodynamic influence coefficient matrix
$\Delta\theta$	Angular spacing of longitudinal filaments
Δx_r	Axial spacing of vortex rings
$\Delta\vec{s}$	Helix displacement vector
ϵ	Wing section twist
η	Vortex core smoothing function
Γ	Vortex circulation strength
γ	Linear circulation density
$\hat{n}$	Panel unit normal vector
$\hat{t}$	Unit vector of trailing vorticity
λ	Wing taper ratio
Λ_{LE}	Wing leading edge sweep angle
ω	Angular velocity
ϕ	Helix angle

ρ	Freestream air density
θ	Angular coordinate
$\vec{a}$	Vector from a point to start of vortex segment
$\vec{b}$	Vector from a point to end of vortex segment
$\vec{e}$	Vortex segment end point
$\vec{q}_1$	Biot-Savart law function for a finite-length vortex line
$\vec{q}_2$	Biot-Savart law function for a semi-infinite vortex line
$\vec{r}$	Position vector of a velocity calculation point
$\vec{s}$	Vortex segment starting point
$\vec{V}_i$	Induced velocity vector
$\vec{V}_w$	Wing-induced velocity
A	Propeller reference area
b	Wing span
c	Wing chord
C_L	Wing lift coefficient
C_l	Section lift coefficient
c_r	Wing root chord
C_T	Thrust coefficient, defined as $C_T = T/(\rho n^2 D^4)$
C_T^*	Thrust coefficient, defined as $C_T^* = 2T/(\rho V_\infty^2 A)$
$C_{D,i}$	Wing induced drag coefficient
$C_{d,i}$	Section induced drag coefficient

D	Propeller diameter
$d\vec{F}$	Differential force on a wing section
d_r	Direction of rotation
d_t	Direction of thrust
ds	Panel bound vortex length
E	Complete elliptic integral of the second kind
J	Propeller advance ratio
K	Complete elliptic integral of the first kind
k	Elliptic modulus
L'	Lift per unit span
L/D_i	Lift-to-induced drag ratio
n	Propeller rotation rate
N_b	Number of propeller blades
N_l	Number of longitudinal vortices
N_p	Number of panels
N_r	Number of ring vortices
N_{rev}	Number of propeller revolutions
p	Helical pitch
R	Propeller radius / vortex ring radius
r	Radial coordinate
r_c	Vortex core radius

r_p Perpendicular distance from a vortex line

S Wing planform area

T Propeller thrust force

V_∞ Freestream velocity

V_θ Tangential induced velocity

V_m Total velocity at the bound vortex midpoint

V_r Vortex ring induced velocity

V_x Axial induced velocity

V_y Horizontal in-plane induced velocity

V_z Vertical in-plane induced velocity

x Axial coordinate

y Spanwise coordinate

z Vertical coordinate

Subscripts

θ Tangential direction; positive counterclockwise

b Bound vortex quantity

h Helix quantity

i Control point / Wing panel index

j Vortex ring index

x Longitudinal direction; positive downstream along propeller axis

y Spanwise direction; positive along starboard wing

z Vertical direction; positive upward

Chapter 1

Introduction

1.1 Background and Motivation

The interactions between propellers and aerodynamic lifting surfaces have been studied extensively due to their importance in aircraft performance and handling. Lifting surfaces immersed in a propeller slipstream are subject to perturbation velocities that modify the magnitude and direction of the inflow, thereby altering the effective angle of attack and loading distributions. Fast and accurate modeling of this interaction has gained increasing attention, especially with recent developments in electric-powered aerial vehicles that employ distributed propulsion systems. Current research in the area of distributed electric propulsion (DEP) seeks to leverage the slipstream effect of multiple propellers along a wing to enhance aerodynamic performance, mitigate noise generation and reduce fuel emissions [1]. Several design concepts have been created to assess these potential benefits. In 2014, NASA launched the Leading Edge Asynchronous Propulsion Technology (LEAPTech) project and tested an experimental wing design with 18 electric motors and propellers for augmented lifting capabilities [2]. This work was succeeded by the SCEPTOR program, which focused on the design of a full-scale distributed propulsion demonstrator [3].

The integration of distributed propulsion systems has also been explored for deployment in the advanced and urban air mobility sectors. In 2023, aerospace startup, Electra, unveiled the EL-2 Goldfinch, a hybrid-electric eSTOL aircraft [4] capable of carrying up to nine passengers with a maximum range of 500 miles. Its design incorporates the blown-air effect of eight propellers distributed along the wing leading edge to increase lifting performance at low speeds, significantly reducing take-off and landing distances. Initial flight tests have exhibited promising results, and the aircraft is under further development with entry into commercial service targeted for 2028.

As part of a long-term campaign to create environmentally sustainable technologies, Airbus is also striving to advance distributed propulsion research through its EcoPulse hybrid-electric demonstrator [5]. In addition to evaluating the aerodynamic, acoustic and energy saving benefits of their design, Airbus is testing an asymmetric flight control system to determine how the operation of six individual propulsion units affects overall aircraft performance. This includes development of a flight computer that can monitor the propulsion system, optimize thrust and reduce drag at the wingtips.

The growing number of programs devoted to electric propulsion research for aeronautical applications has underscored the importance of effectively evaluating overall system performance. A key aspect of this task is the numerical analysis of propeller effects on vehicle aerodynamics. Historically, a wide variety of computational techniques have been developed for modeling propeller flow fields, ranging from simple panel methods to high-fidelity computational fluid dynamics (CFD) simulations. Within this spectrum, advanced approaches may be used to generate comprehensive solutions and capture detailed flow physics, but at significant computational cost. Consequently, low-order models have emerged as attractive options for preliminary design and analysis. Given their reduced computational expense, they can also be used to effectively integrate propeller effects in time-critical applications, such as aerodynamic prediction and flight simulation tools.

This thesis presents a low-order propeller aerodynamic model in which the wake streamtube is represented by a cylindrical mesh of discrete vortex elements in potential flow. The conceptual basis of this modeling approach can be traced back to the early 20th century, during which notable developments in the vortex theory of aerodynamic lifting surfaces were first published. Following creation of the classical momentum theory by Rankine [6] in 1865 and Froude [7] in 1889, aerodynamicists sought alternative methods to analyze

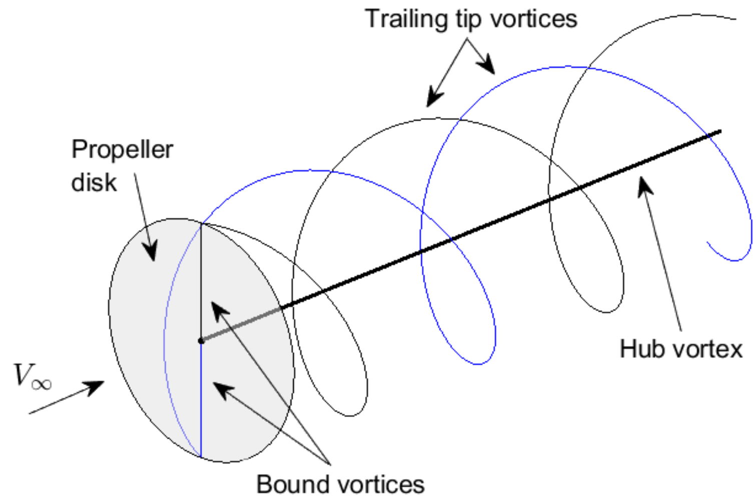

Figure 1.1: Joukowsky rotor vortex model for a 2-bladed propeller.

screw propellers with a finite number of blades. In 1912, Joukowsky [8] published the first in a series of articles that outlined a model for propellers based on a rotating horseshoe vortex system, as depicted in figure 1.1. This wake structure is analogous to the horseshoe vortex model of a finite wing in that each blade is represented as a line of constant bound circulation along the span, giving rise to trailing vortices only at the tips. With regards to the finite wing model, Prandtl [9] extended the horseshoe vortex concept in 1918 by allowing the bound circulation to vary continuously along the span, resulting in the formation of a trailing vortex sheet behind the wing. By relating the induced-angle-of-attack distribution caused by the vortex system with the spanwise bound circulation along the wing, Prandtl established the lifting-line theory, which forms the basis of many numerical vortex lattice methods (VLM), including the Weissinger method [10] used in this thesis.

Early rotor vortex theories were later supplemented by a number of studies that analyzed the helical vortex structures formed by the combined translational and rotational motion of the blades. A comprehensive treatment of the subject was presented in 1936 by Kawada [11], who devised approximate formulas for the velocity induced by a thin, infinite helical vortex in an incompressible and inviscid flow. In 1982, Hardin [12] independently derived and published similar solutions for the induced velocity in terms of infinite Kapteyn series containing modified Bessel functions. More recently, the mathematical properties of these solutions have been examined for their accuracy in modeling the propeller slipstream [13].

Due to the complex geometry of helical lines, a general closed-form solution for the induced velocities of a helical vortex system does not currently exist. However, these velocities can be estimated by discretizing the helices into straight-line segments, applying the Biot-Savart law to each individual segment and integrating the contributions from the entire system. The accuracy of this method was evaluated by Gupta and Leishman [14], who compared the induced velocity distributions of a discretized helix with those of a corresponding vortex ring for different combinations of helical pitch, skew and number of turns. In a systematic series of test cases, both models generated velocity fields that were second-order accurate with respect to the angular discretization of the vortices, provided that the segments were adequately small. It was also concluded that the vortex ring could be treated as a special case of the helical vortex in the limit that the helical pitch tends to zero. The discretized helical vortex concept has been utilized to model propeller-wing interactions [15], with predictions of the wing loading matching relatively well with higher-order methods and experimental data.

Although it contains its own merits, the discretized helical wake model requires a relatively fine segmentation of the vortices for an accurate solution, which can be computationally expensive and restrictive for quick predictions of the slipstream velocities. This thesis aims to demonstrate an approach for faster computations whereby a time-averaged helical vortex wake is decomposed into a system of circular vortex rings and rectilinear vortices along the longitudinal direction, as shown in figure 1.2. These elementary vortex structures exhibit no torsion and are therefore simpler to treat than a helix [16]. To this point, Lewis [17] showed that, by applying the Biot-Savart law and invoking spatial symmetry arguments, the influence of circular vortex rings can be readily expressed using analytical relations involving complete elliptic integrals. Due to their simplicity, these solutions have been used for a variety of modeling applications. For example, both van Heemst et al. [18] and Meghlaoui et al. [19] used circular vortex rings to calculate axial induced velocities in the wakes of horizontal-axis wind turbines and obtained reasonable agreement with experimental data. In another study, Bontempo and Manna [20] developed a free-wake vortex ring model to iteratively compute the strength and shape of a non-rotating slipstream for a uniformly-loaded propeller. This approach was verified using a CFD actuator disk model [21] and performed well in predicting the axial induced velocities at low to moderate thrust coefficients, with increasing numerical error at higher propeller loadings. Despite this limitation, the vortex ring model does not require a numerical approximation and is used in this thesis for its computational efficiency.

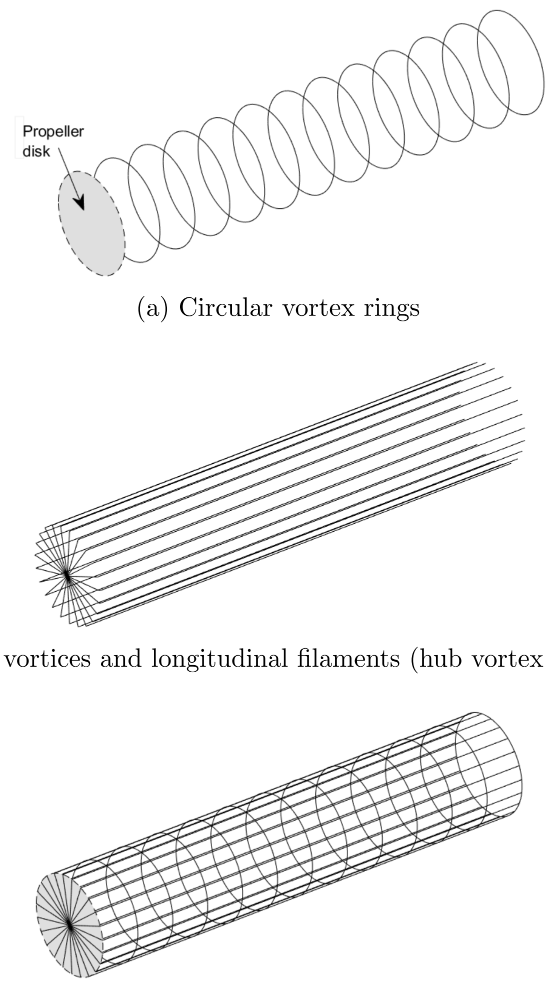

(a) Circular vortex rings

(b) Bound vortices and longitudinal filaments (hub vortex not shown)

(c) Combined vortex system (hub vortex not shown)

Figure 1.2: Discretized components of the cylindrical wake vortex model.

Additionally, in the current modeling scheme, the slipstream does not contract and is represented by a discretized cylindrical vortex sheet of constant diameter. A similar type of wake structure was studied by Branlard and Gaunaa [22], who calculated the induced velocity field from a cylindrical vortex system of uniform circulation as a simple model for wind turbines with finite tip-speed ratios. Under the assumption of a constant-diameter wake, the axial vorticity can be discretized into semi-infinite rectilinear filaments, further simplifying the calculation of the tangential induced velocity using the Biot-Savart law. This configuration of vortex elements limits the flexibility of the model in certain cases, including static and low-advance-ratio flight, where slipstream contraction is significant. By contrast, the wake contraction is small for propellers operating at high advance ratios due to the relative dominance of the freestream velocity over the induced axial velocity in the slipstream. For this reason, the current model can be useful in the analysis of lightly or moderately-loaded propellers, for which the disk loading is exactly or approximately uniform. The extension of the current method to incorporate a wake contraction model is posited as future work.

1.2 Objectives

The objective of this thesis is to develop a low-order propeller wake model and demonstrate its ability to efficiently calculate induced axial and tangential velocities in the slipstream. In this model, the time-averaged wake of a uniformly-loaded propeller is represented by a vortex cylinder, which is discretized into a mesh-like system of circular vortex rings and semi-infinite longitudinal filaments. For a given propeller geometry and operating condition, the configuration of the wake vortex elements is represented using aerodynamic influence coefficient (AIC) matrices. The strengths of the vortex elements are estimated by decomposing the wake circulation of an equivalent helical vortex system into an axial and tangential component. Using this method, the propeller-induced velocities are calculated in the slipstream, and convergence studies are conducted to identify the effect of relevant wake discretization parameters.

The propeller wake model is also coupled with the Weissinger lifting-line method to investigate aerodynamic interactions for propeller-wing configurations. This work aims to demonstrate the localized and aggregate aerodynamic influence of a propeller on a downstream wing immersed in the slipstream, with a focus on changes to the lift and induced drag. The combined low-order model is validated against higher-fidelity methods and experimental data in order to assess its accuracy and limitations for various propeller-wing geometries and operating conditions.

Chapter 2

Theoretical Development

2.1 Propeller Wake Model

The propeller wake model is based on Joukowsky's rotor vortex theory [16] for uniformly-loaded propellers in axial flight. As described in section 1.1, this model is comparable in concept to the horseshoe vortex representation of a finite wing. For an N_b-bladed propeller immersed in a steady, inviscid and incompressible flow, the bound vorticity distribution is concentrated into thin vortex filaments of constant circulation along each blade. It is a necessary requirement, in accordance with Helmholtz's second theorem, that these vortex lines extend to infinity downstream of the propeller at both the hub and blade tips. This results in a vortex system consisting of a semi-infinite hub vortex with circulation strength Γ_{hub}, along with N_b bound vortices along the blades, each with strength Γ_{hub}/N_b that trail into the far-wake as semi-infinite tip vortices of the same strength. Figure 2.1 depicts the components of the wake system with their corresponding circulation strengths. To ensure that the wake vorticity is conserved—a stipulation of Helmholtz's first theorem—the circulation of the hub vortex is directed opposite the circulation of the trailing tip vortices. A more detailed treatment of the scheme used to determine the direction of circulation is presented in section 2.1.3.

The exact configuration of the wake vortex structure depends on the propeller geometry and flight operating conditions. A variety of factors affect the shape and strength of the

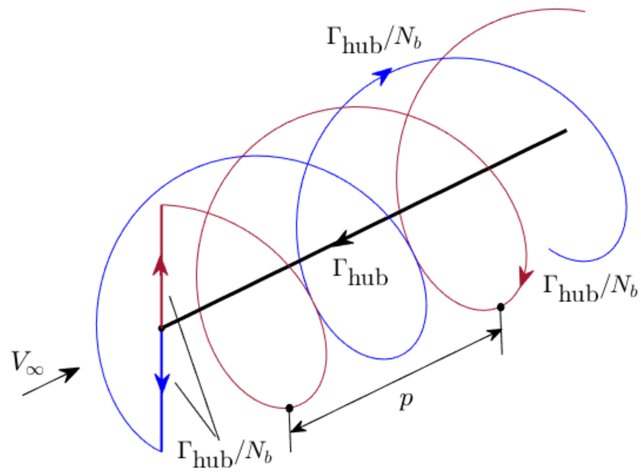

Figure 2.1: Circulation strength magnitudes of the hub, bound and trailing helical vortices.

vortex elements; however, the intention with the current model is to simplify the description of the wake by reducing the number of necessary inputs. To this aim, the model accepts general parameters including flight speed, propeller position, diameter, number of blades, thrust coefficient, thrust direction, rotation speed (RPM), and rotation direction. Multiple propellers with different operating conditions can also be handled.

In axial flight, the propeller blades advance at a rate equal to the freestream velocity V_∞ and rotate about the hub at a rate of n revolutions per second. For a propeller of diameter D, the advance ratio is defined as

$$J = \frac{V_\infty}{nD} \tag{2.1}$$

Due to the combined translation and rotation of the propeller blades, each trailing tip vortex forms the shape of a helix. A characteristic parameter of these helical lines is the pitch p, which is the axial displacement of the helix over a single revolution. Given that the time taken for a single blade revolution is $\Delta t_{\text{rev}} = 1/n$, the helical pitch is related to the advance ratio by

$$p = JD \tag{2.2}$$

Equation 2.2 shows that for a propeller of fixed geometry, the axial spacing of the helical filaments is directly proportional to the advance ratio, assuming no slip. This spacing is also related to the angle ϕ formed by the helix with the propeller axis:

$$\phi = \tan^{-1}\left(\frac{2\pi R}{p}\right) \tag{2.3}$$

where R is the propeller radius. In the approximate case of a constant-diameter wake, which is the focus of this thesis, the trailing helices do not contract along the streamwise direction. Under this assumption, the helix angle is constant throughout the wake.

A propeller operating in axisymmetric flight sustains a pressure difference that gives rise to a thrust force T directed along the direction of flight. This force is quantified by a non-dimensional thrust coefficient, which is typically defined as

$$C_T = \frac{T}{\rho n^2 D^4} \tag{2.4}$$

where ρ is the freestream air density. However, the wake model in this thesis adopts an alternative definition of the thrust coefficient from McCormick [23], which is given by

$$C_T^* = \frac{T}{\frac{1}{2}\rho V_\infty^2 A} \tag{2.5}$$

where A is chosen as the area of the annular ring formed by excluding the asymmetric hub region. By approximating the propeller as a circular disk with an axisymmetric hub of diameter D_{hub},

$$A = \frac{\pi}{4}(D^2 - D_{\text{hub}}^2) \tag{2.6}$$

To facilitate comparisons with existing propeller data, the standard definition of C_T in equation 2.4 is used as a model input and converted to the corresponding value of C_T^* using the following relation:

$$C_T^* = \frac{8}{\pi J^2}\left(\frac{D^2}{D^2 - D_{\text{hub}}^2}\right) C_T \tag{2.7}$$

In this analysis, a time-averaged wake model is used for capturing the mean effects of

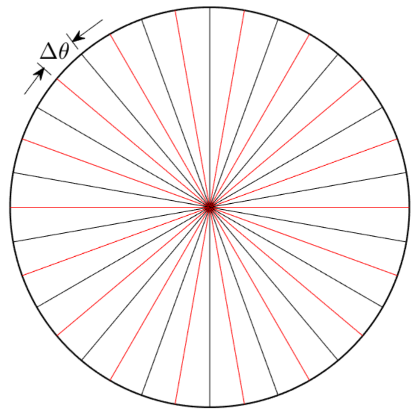

(a) Superposition of bound vortices at each blade angle over a single revolution (front view)

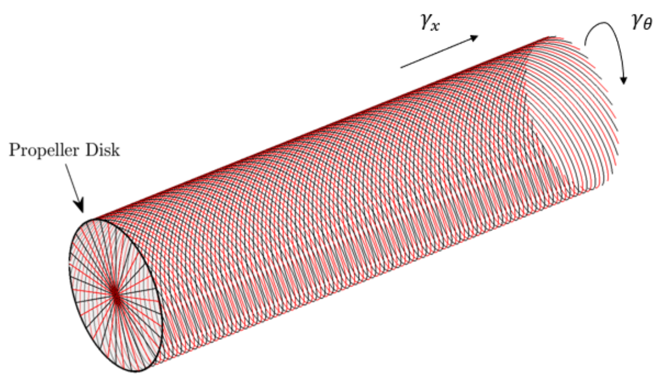

(b) Superposition of bound and trailing vortices at each blade angle

Figure 2.2: Depiction of a time-averaged helical vortex streamtube with a blade sweep of $\Delta\theta = 10°$.

the propeller during steady state operation. This concept is outlined by considering that at any point in time, the trailing helical vortices occupy discrete positions in space based on the instantaneous orientation of the blades. By rotating the blades through small intervals, as demonstrated in figure 2.2 for an angular spacing of $10°$, the positions of the helices are shifted, and the corresponding instantaneous velocities in the slipstream can be calculated. The averaged velocities are obtained by summing the instantaneous velocities for multiple blade angles over a complete revolution and dividing by the number of intervals. As the angular step tends to zero, the rotation of the trailing wake system forms a cylindrical vortex sheet containing both axial and tangential vorticity [24]. In the current model, this cylindrical structure is discretized into circular vortex rings and semi-infinite rectilinear filaments, as detailed in the next section.

2.1.1 Cylindrical Vortex Decomposition

The circular rings and semi-infinite rectilinear filaments used in this model are elementary vortex elements with well-established properties [16]. A particular advantage of these vortex structures is that their influence on the velocity field can be expressed in terms of their geometric configuration and scaled by the corresponding vortex strength.

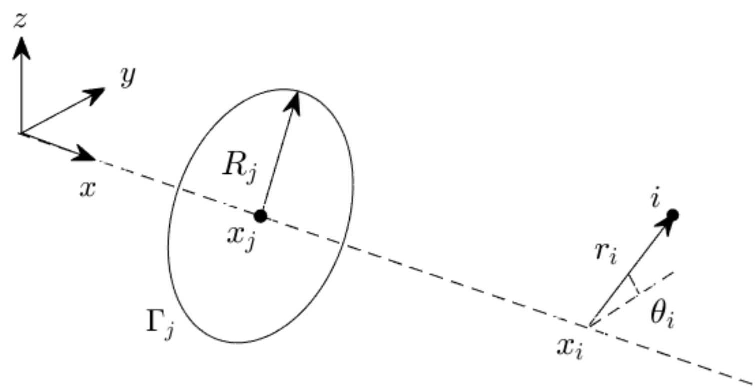

Figure 2.3: Setup for calculating the velocity induced by vortex ring j on a point i in the flow field.

Figure 2.3 illustrates the setup used to calculate the velocity induced by an axisymmetric vortex ring j on an arbitrary point i in the flow field. Lewis [17] derives equations for the ring-induced velocity components in terms of non-dimensional coordinates. The corresponding dimensional forms are given by

$$V_{x_{ij}} = \frac{\Gamma_j}{2\pi\sqrt{(x_i - x_j)^2 + (r_{ij} + R_j)^2}} \left[K(k_{ij}^2) + \frac{R_j^2 - r_{ij}^2 - (x_i - x_j)^2}{(x_i - x_j)^2 + (R_j - r_{ij})^2} E(k_{ij}^2) \right] \tag{2.8}$$

$$V_{r_{ij}} = \frac{\Gamma_j (x_i - x_j)}{2\pi r_{ij}\sqrt{(x_i - x_j)^2 + (r_{ij} + R_j)^2}} \left[K(k_{ij}^2) - \frac{R_j^2 + r_{ij}^2 + (x_i - x_j)^2}{(x_i - x_j)^2 + (R_j - r_{ij})^2} E(k_{ij}^2) \right] \tag{2.9}$$

where Γ_j and R_j are the vortex strength and radius, respectively, of the jth vortex ring,

r_{ij} is the radial coordinate of the ith velocity calculation point with respect to the center of the jth vortex ring, K and E are the complete elliptic integrals of the first and second kinds, respectively, and k is the elliptic modulus, which is defined as

$$k_{ij} = \sqrt{\frac{4 r_{ij} R_j}{(x_i - x_j)^2 + (r_{ij} + R_j)^2}} \tag{2.10}$$

The elliptic integrals are evaluated using a vectorized implementation of the *ellipke* function in MATLAB. From figure 2.3, the point with Cartesian coordinates (x_i, y_i, z_i) has corresponding radial and angular coordinates, measured relative to the center of vortex ring j, given by

$$r_{ij} = \sqrt{(y_i - y_j)^2 + (z_i - z_j)^2} \tag{2.11}$$

and

$$\theta_{ij} = \tan^{-1}\left(\frac{z_i - z_j}{y_i - y_j}\right) \tag{2.12}$$

The angular values are computed using the four-quadrant inverse tangent to ensure that the coordinates are resolved in the correct position. In this work, x is positive downstream along the propeller axis, y is positive along the starboard wing, and z is positive vertically upwards.

To model the axial induced velocity in the slipstream, a series of equally-spaced circular vortex rings are aligned along the propeller axis, as illustrated in figure 1.2. The number of rings N_r in the wake and the desired number of propeller revolutions N_{rev} (used to model a desired slipstream distance downstream of the propeller) are specified as user inputs. These values are used together to define a constant ring spacing Δx_r along the axis:

$$\Delta x_r = p\left(\frac{N_{\text{rev}}}{N_r}\right) \tag{2.13}$$

where p is the helical pitch defined in equation 2.2. Using this definition, the vortex rings are systematically generated in proportion to the advance ratio.

The number of longitudinal vortices N_l is also supplied as an input to the model.

These vortices are distributed uniformly around the circumferential extent of the slipstream. Without wake contraction, the longitudinal vortices are rectilinear and extend from the plane of the propeller towards downstream infinity. As a result, the induced velocity from these vortex elements is calculated using a vectorized formulation of the Biot-Savart law:

$$\vec{V}_i = \frac{\Gamma_x}{4\pi}\vec{q}_2(\vec{r}, \vec{s}, \hat{t}) \tag{2.14}$$

where Γ_x is the vortex strength of a single longitudinal filament, $\vec{s}$ is the position vector of the starting point of that filament, $\vec{r}$ is the position vector of a velocity calculation point, $\hat{t}$ is a unit vector pointing in the direction of trailing vorticity, and $\vec{q}_2$ is the vectorized Biot-Savart function for a semi-infinite vortex line, defined as

$$\vec{q}_2 = \frac{\vec{a} \times \hat{t}}{(\vec{a} \times \hat{t}) \cdot (\vec{a} \times \hat{t})}\left(1 - \frac{\vec{a} \cdot \hat{t}}{|\vec{a}|}\right)\eta \tag{2.15}$$

In equation 2.15, $\vec{a}$ is the vector from $\vec{r}$ to $\vec{s}$. By inspection, a singularity exists when the velocity is calculated on the vortex line itself. To account for this, $\vec{q}_2$ is desingularized using the Lamb-Oseen vortex core model [25], which simulates a finite core of radius r_c using the smoothing function

$$\eta = 1 - e^{-(r_p/r_c)^2} \tag{2.16}$$

where r_p is the perpendicular distance from the velocity calculation point to the vortex line. By considering the defined vector geometry, the magnitude of this perpendicular distance is

$$r_p = \frac{|(\vec{e} - \vec{s}) \times (\vec{s} - \vec{r})|}{|\vec{e} - \vec{s}|} \tag{2.17}$$

where $\vec{e}$ denotes the end of a vortex segment. For the semi-infinite filaments, the endpoint is calculated as $\vec{e} = \vec{s} + \hat{t}$.

In addition to the influence of the trailing vortices, the velocities induced by the hub vortex are also computed from equation 2.14 by substituting Γ_{hub} for Γ_x. The induced velocities from the bound vortices of strength Γ_b are calculated in similar fashion, with the exception that the Biot-Savart function $\vec{q}_1$ for a finite-length vortex line is used:

$$\vec{V}_i = \frac{\Gamma_b}{4\pi}\vec{q}_1(\vec{r}, \vec{s}, \vec{e}) \tag{2.18}$$

Here, $\vec{q}_1$ is defined as

$$\vec{q}_1 = \frac{\vec{a} \times \vec{b}}{(\vec{a} \times \vec{b}) \cdot (\vec{a} \times \vec{b})} \left(|\vec{a}| + |\vec{b}|\right) \left(1 - \frac{\vec{a} \cdot \vec{b}}{|\vec{a}||\vec{b}|}\right) \eta \tag{2.19}$$

As before, equation 2.19 is multiplied by the smoothing function η from the Lamb-Oseen model to prevent calculation of singular velocity values.

2.1.2 Vortex Circulation Strength

For the discretized cylindrical wake, the total circulation strength is decomposed into an axial and tangential vorticity component. This procedure follows a method outlined by Branlard and Gaunaa [22], in which the total circulation over a single helix revolution, as shown in figure 2.4, is considered. Due to the combined translation and rotation of the propeller blades, the arc length swept by a helix over a complete revolution is given in vector form by

$$\Delta\vec{s} = p\hat{\boldsymbol{e}}_x + 2\pi R\hat{\boldsymbol{e}}_\theta \tag{2.20}$$

The linear circulation densities of the tangential and axial vortex elements are obtained by dividing the total hub circulation strength by the helical displacement perpendicular to the respective vorticity component. That is,

$$\gamma_\theta = \frac{\Gamma_{\text{hub}}}{p} \tag{2.21}$$

$$\gamma_x = \frac{\Gamma_{\text{hub}}}{2\pi R} \tag{2.22}$$

where Γ_{hub} is the product of the number of blades N_b and the vortex strength Γ_h of a single helix:

$$\Gamma_{\text{hub}} = N_b \Gamma_h \tag{2.23}$$

Comparing equations 2.21 and 2.22 with equation 2.3, the magnitudes of the vortex strength density components are related through the helix angle as follows:

$$\frac{\gamma_\theta}{\gamma_x} = \tan\phi \tag{2.24}$$

The circulation density of the vortex rings is determined from a derivation by Bontempo and Manna [20], who related the tangential vortex strength of a contracting wake to the difference in static pressure across the propeller disk. From this process, it was found that the tangential circulation density converges to a uniform value where the wake diameter becomes effectively constant. This value is used as an estimate in the current model and is given by

$$\gamma_\theta = V_\infty \left(1 - \sqrt{1 + C_T^*}\right) \tag{2.25}$$

With the assumptions of a uniformly-loaded propeller and constant-diameter slipstream, the linear circulation densities of the axial and tangential vortex systems are constant throughout the wake. Furthermore, without slipstream contraction, the helix angle does not change. Thus, the circulation density of the longitudinal vortex filaments is determined by combining equations 2.24 and 2.25.

The vortex ring circulation strength is obtained by multiplying the tangential circulation density in equation 2.21 with the ring spacing Δx_n calculated from equation 2.13, as follows:

$$\Gamma_\theta = \gamma_\theta \Delta x_r = \left(\frac{N_b \Gamma_h}{p}\right) \Delta x_r \tag{2.26}$$

A similar calculation is used to find the strength of the longitudinal vortices, which are spaced by arc length $R\Delta\theta$:

$$\Gamma_x = \gamma_x R \Delta\theta \tag{2.27}$$

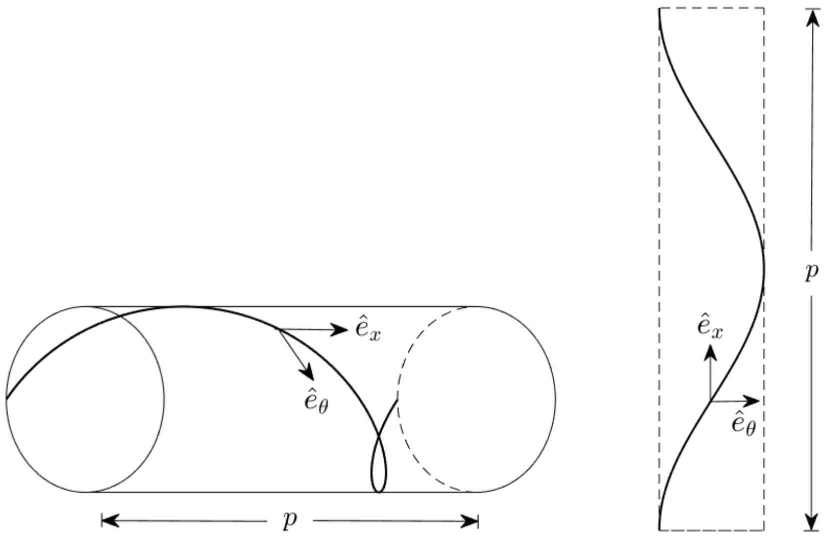

(a) Side view (b) Top view

Figure 2.4: Helical vortex decomposition into axial and tangential components.

A constant angular spacing is defined based on the number of prescribed longitudinal filaments:

$$\Delta\theta = \frac{2\pi}{N_l} \tag{2.28}$$

Combining equations 2.22, 2.23, 2.27, and 2.28 gives an estimate of the longitudinal vortex strength as

$$\Gamma_x = \left(\frac{N_b}{N_l}\right)\Gamma_h \tag{2.29}$$

2.1.3 Circulation Direction Scheme

The thrust direction d_t and propeller rotation direction d_r are included as inputs to the propeller wake model. These inputs can take two possible values: 1 or -1. A convention is established to differentiate the vortex circulation directions for different combinations of d_r and d_t. For consistency, rotation directions in this model are specified relative to a reference point behind the propeller; that is, the direction of spin is interpreted when viewed into the upstream direction. Given a prescribed direction of the thrust force and blade

Table 2.1: Circulation sign convention for each combination of thrust and rotation directions.

	d_t	d_r	Γ_b	Γ_{hub}	Γ_x	Γ_θ
Propeller, CW	1	1	+	+	+	+
Propeller, CCW	1	−1	−	−	−	+
Wind Turbine, CW	−1	1	−	−	−	−
Wind Turbine, CCW	−1	−1	+	+	+	−

rotation, the appropriate direction of the bound vortex circulation is found by applying a generalized form of the Kutta-Joukowski theorem. In this process, the cross product of the flow velocity relative to the blade and bound vorticity vector should result in a thrust vector whose direction corresponds to the desired "propeller" or "wind turbine" case. Based on the determined orientation of the bound vortex circulation, the directions of all other vortex circulations can be resolved in accordance with Helmholtz's theorems.

In the established convention, a thrust-producing propeller rotating clockwise is chosen as the baseline case where all vortex circulations are positive; this corresponds to $d_t = 1$ and $d_r = 1$. It follows that Γ_{hub} is positive along the upstream direction, Γ_b is positive from hub to blade tip, Γ_x is positive along the downstream direction, and Γ_θ is positive along the counterclockwise direction. Setting $d_t = -1$ generates a wind turbine wake, whereas $d_r = -1$ sets the rotation direction to counterclockwise. Table 2.1 summarizes the effect of d_t and d_r on the signs of the wake vortex elements. These cases are visualized in Figure 2.5, which includes depictions of the thrust T and induced axial velocity V_i. Figures 2.5a and 2.5b correspond to a thrust-producing propeller in which the axial induced velocity increases in the slipstream, and figures 2.5c and 2.5d represent a wind turbine configuration where the slipstream axial velocity is reduced. Figure 2.6 shows each case for the decomposed helical vortex wake of a 2-bladed rotor.

2.2 Wing Aerodynamic Model

The wing aerodynamics are modeled using the Weissinger method [10], which is a modified vortex lattice method based on Prandtl's lifting-line theory [9]. In this model, the chordwise vorticity of a finite wing is concentrated into a bound vortex line along the quarter-chord.

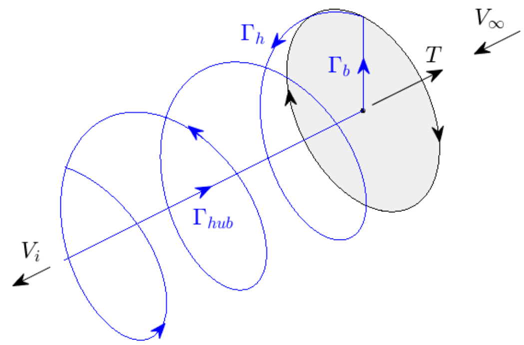

(a) Propeller, clockwise

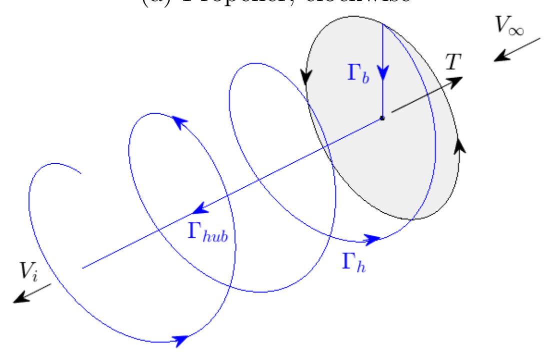

(b) Propeller, counterclockwise

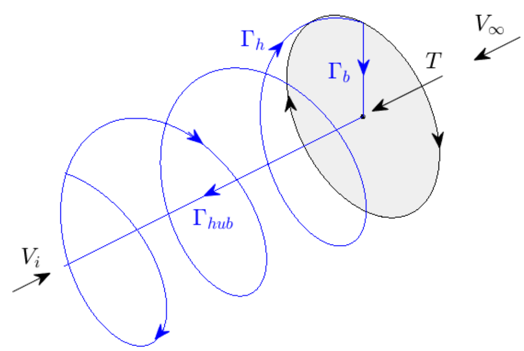

(c) Wind turbine, clockwise

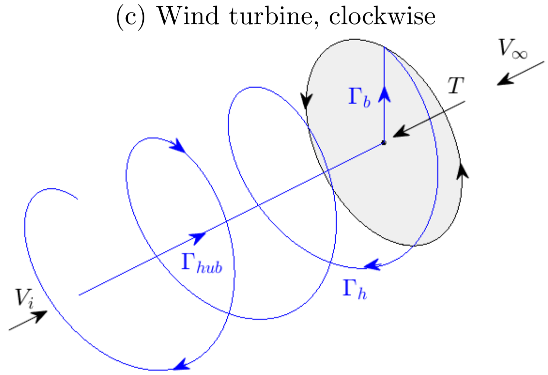

(d) Wind turbine, counterclockwise

Figure 2.5: Vortex systems corresponding to propeller and wind turbine cases with clockwise and counterclockwise rotation.

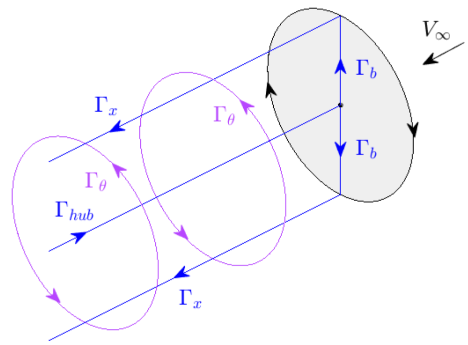

(a) Propeller, clockwise

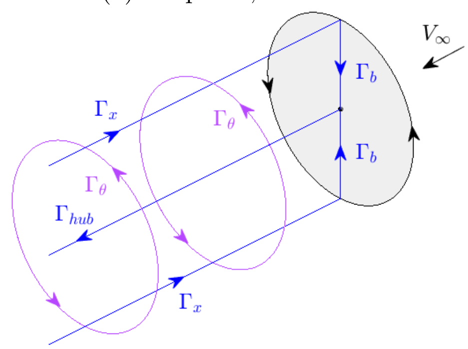

(b) Propeller, counterclockwise

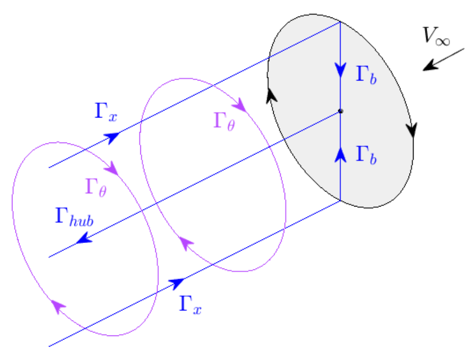

(c) Wind turbine, clockwise

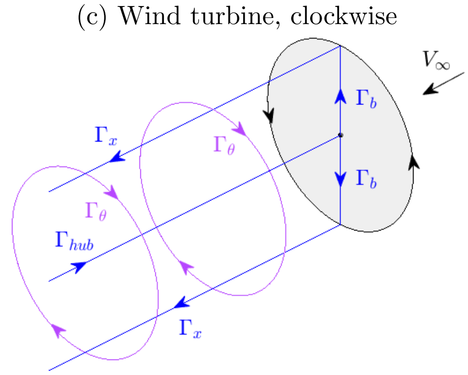

(d) Wind turbine, counterclockwise

Figure 2.6: Vortex systems for the decomposed wake of a 2-bladed propeller and wind turbine with clockwise and counterclockwise rotation.

The associated circulation Γ along the bound vortex is related to the elemental force per unit span on a two-dimensional airfoil section by the Kutta-Joukowski theorem:

$$d\vec{F}' = \rho(\vec{V} \times \vec{\Gamma}) \tag{2.30}$$

To capture the spanwise variation of aerodynamic loads, the bound vortex is discretized into finite-length segments of variable circulation strength. In compliance with Helmholtz's theorems, the change in circulation between each segment results in the formation of a trailing horseshoe vortex system. The superposition of these horseshoe vortices produces an arrangement of vortex lattice panels, each with a bound vortex segment and a pair of trailing vortex legs, as shown in figure 2.7.

The aerodynamic influence of the wing vortex system is determined by first obtaining a solution for the vortex lattice strengths. This is achieved by satisfying the appropriate boundary condition along the wing surface. For potential flow, the customary boundary condition at a surface interface is the zero-normal-flow condition, which requires the net normal velocity to vanish along the wing surface [26]. In the Weissinger method, this condition is enforced at prescribed control points along the 3/4-chord line. Considering the wing alone, the net velocity at each control point consists of the freestream and wake-induced component $\vec{V}_w$, such that the boundary condition becomes

$$(\vec{V}_\infty + \vec{V}_w) \cdot \hat{n} = 0 \tag{2.31}$$

where $\hat{n}$ is the unit normal vector of a panel.

The choice to model the bound vortex along the quarter-chord and enforce the boundary condition along the 3/4-chord is a feature of the Weissinger method that distinguishes it from lifting-line theory. A limitation of the latter is that the induced velocities are calculated on the bound vortex line itself. In the case of a swept wing, where the bound vortex is not straight, this causes the nonphysical result of infinite induced velocity on the lifting line. By contrast, the Weissinger method can acommodate swept wings since the velocities are calculated on the 3/4-chord line, which is offset from the bound vortex.

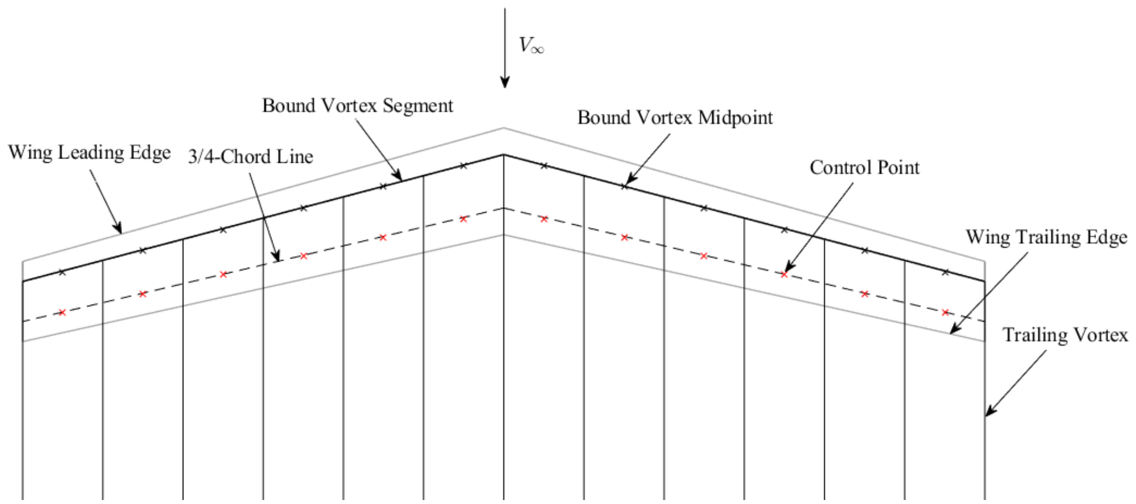

Figure 2.7: The discrete vortex lattice wing geometry used in the Weissinger method.

The specific use of the quarter-chord and 3/4-chord lines in the Weissinger method is based on the application of a 2-D lumped vortex method, which solves for the flow past a thin cambered airfoil with chord c by concentrating the bound vortex at an arbitrary chordwise position a and satisfying flow tangency at a different chordwise point b. These locations are found by incorporating the analytical circulation for a parabolic camberline from thin airfoil theory into the flow tangency boundary condition. It can be shown that for the resulting solution to be valid at any angle of attack and camber geometry, $a = c/4$ and $b = 3c/4$.

In the current implementation of the Weissinger method, the wing planform is defined by discrete patches, which are used to specify chord, zero-lift angle of attack, and linear twist distributions along the span. For each patch, the number of lattices is prescribed separately, allowing for variable lattice densities depending on the patch size.

2.3 Combined Model

The combined model integrates the propeller effects into the Weissinger method by accounting for the slipstream velocities at the wing control points and bound vortex midpoints. Figure 2.8 illustrates the influence of a vortex ring on the velocity at a control point. A depiction of the combined model for an example propeller-wing system is shown in figure 2.9, and the calculation procedure is outlined in figure 2.10.

In the propeller wake model, the velocities induced by the vortex rings and rectilinear filaments are calculated separately. The cumulative influence of the vortex rings is calculated by applying equations 2.8 and 2.9 at each control point and assembling the geometric terms into coefficient matrices $\boldsymbol{F}_x$ and $\boldsymbol{F}_r$, each of size $N_p \times N_r$, for the respective axial and in-plane velocities:

$$\vec{V}_{x,\text{ring}} = \boldsymbol{F}_x \vec{\Gamma}_\theta \tag{2.32}$$

$$\vec{V}_{y,\text{ring}} = \left(\boldsymbol{F}_r \odot \cos\boldsymbol{\theta}\right) \vec{\Gamma}_\theta \tag{2.33}$$

$$\vec{V}_{z,\text{ring}} = \left(\boldsymbol{F}_r \odot \sin\boldsymbol{\theta}\right) \vec{\Gamma}_\theta \tag{2.34}$$

where $\odot$ denotes element-wise matrix multiplication, $\boldsymbol{\theta}$ is a $N_p \times N_r$ matrix containing the angular orientations of the in-plane velocity vectors, approximated from equation 2.12, and $\vec{\Gamma}_\theta$ is a $N_r \times 1$ vector of the vortex ring circulation strengths. These velocities are added

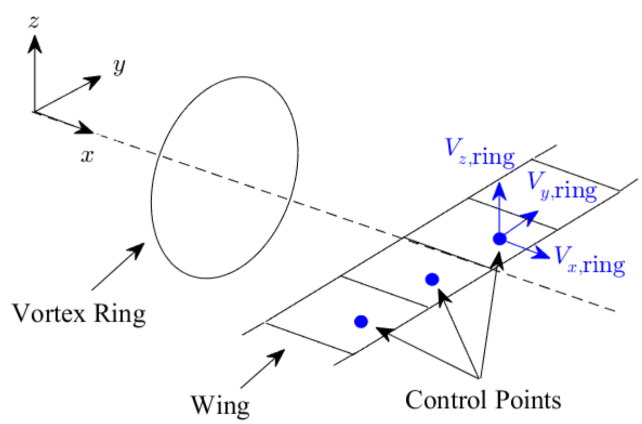

Figure 2.8: Components of velocity induced by a vortex ring at a control point.

to those induced by the rectilinear hub, bound, and trailing vortices to obtain the net propeller velocity $\vec{V}_{\text{prop}}$ at each control point.

The mutual influence of the wing horseshoe vortices on each control point is expressed as an aerodynamic influence coefficient matrix $\boldsymbol{F}_w$. For a wing discretized into N_p panels, $\boldsymbol{F}_w$

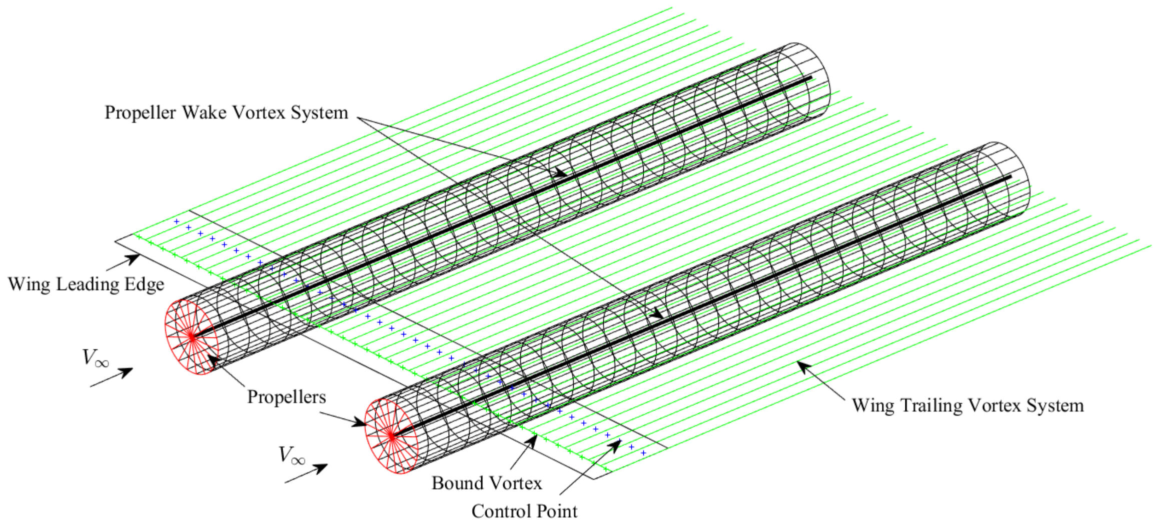

Figure 2.9: Combined model representation for an example propeller-wing system.

is a square $N_p \times N_p$ matrix. The corresponding normal component of induced velocity at each control point is $\boldsymbol{F}_w\vec{\Gamma}$, where $\vec{\Gamma}$ is a $N_p \times 1$ vector of the vortex lattice strengths, whose solution is obtained by imposing the flow tangency boundary condition. In the combined model, the boundary condition is a modified version of equation 2.31 that accounts for the additional velocities induced by the propeller at the ith control point:

$$(\vec{V}_{\text{wing},i} + \vec{V}_{\infty,i} + \vec{V}_{\text{prop},i}) \cdot \hat{n}_i = 0 \tag{2.35}$$

For convenience, equation 2.35 is recast by separating the wing-induced velocities from the freestream and propeller contributions. Upon rearranging the terms and evaluating the normal component of each velocity contribution,

$$V_{n,\text{wing},i} = -V_\infty \sin(\alpha_{g,i} + \epsilon_i - \alpha_{0l,i}) - V_{n,\text{prop},i} \tag{2.36}$$

where α_g is the wing geometric angle of attack (which takes into account section dihedral), ϵ is the wing section twist and α_{0l} is the section zero-lift angle of attack. Applying equation 2.36 at each control point yields a linear matrix equation of the form

$$\boldsymbol{F}_w\vec{\Gamma} = \vec{V}_n \tag{2.37}$$

where $\vec{V}_n$ is an $N_p \times 1$ vector containing the right-hand side of equation 2.36, as applied to all N_p control points. In the current model, a solution for equation 2.37 is found by utilizing the left array division operator in MATLAB.

With the known vortex lattice strengths, the wing loading is determined by calculating the total velocity $\vec{V}_m$ at the bound vortex midpoints. From equation 2.30, the differential force per unit span generated on the ith panel is

$$d\vec{F}_i' = \rho\left(\vec{V}_{m,i} \times \hat{ds}_i\right)\Gamma_i \tag{2.38}$$

where $\hat{ds}$ is the unit vector along a bound vortex segment.

For each panel, the local force is decomposed into the section lift, which is directed perpendicular to the freestream in the plane of the wing section, and the induced drag, which is directed along the freestream. A non-dimensional section lift coefficient is obtained by dividing the local lift per unit span by the product of the dynamic pressure and local chord length, giving

$$C_{l_i} = \frac{2\Gamma_i}{V_\infty^2 c_i}\left[(\vec{V}_{m,i} \times \hat{ds}_i) \cdot \hat{\boldsymbol{e}}_{l_i}\right] \tag{2.39}$$

where $\hat{\boldsymbol{e}}_{l_i}$ is the unit vector perpendicular to the local freestream velocity at the ith panel. Likewise, the section induced drag coefficient is

$$(C_{d,i})_i = \frac{2\Gamma_i}{V_\infty^2 c_i}\left[(\vec{V}_{m,i} \times \hat{ds}_i) \cdot \hat{\boldsymbol{e}}_{d_i}\right] \tag{2.40}$$

where $\hat{\boldsymbol{e}}_{d_i}$ is the unit vector parallel to the local freestream velocity at the ith panel. The total wing lift and induced drag coefficients are calculated as chord-weighted averages of the C_l and $C_{d,i}$ distributions, respectively, across all N_p panels:

$$C_L = \frac{1}{S}\sum_{i=1}^{N_p} c_i ds_i C_{l_i} \tag{2.41}$$

$$C_{D,i} = \frac{1}{S}\sum_{i=1}^{N_p} c_i ds_i (C_{d,i})_i \tag{2.42}$$

where S is the wing planform area. For the inviscid analysis considered in this work, the overall aerodynamic performance of a propeller-wing system is evaluated from the lift-to-induced drag ratio:

$$L/D_i = \frac{C_L}{C_{D,i}} \tag{2.43}$$

Using the obtained spanwise load distributions and integrated loads, the localized and aggregate effects of the propeller slipstream on the wing aerodynamics can be determined to evaluate overall changes to the system performance.

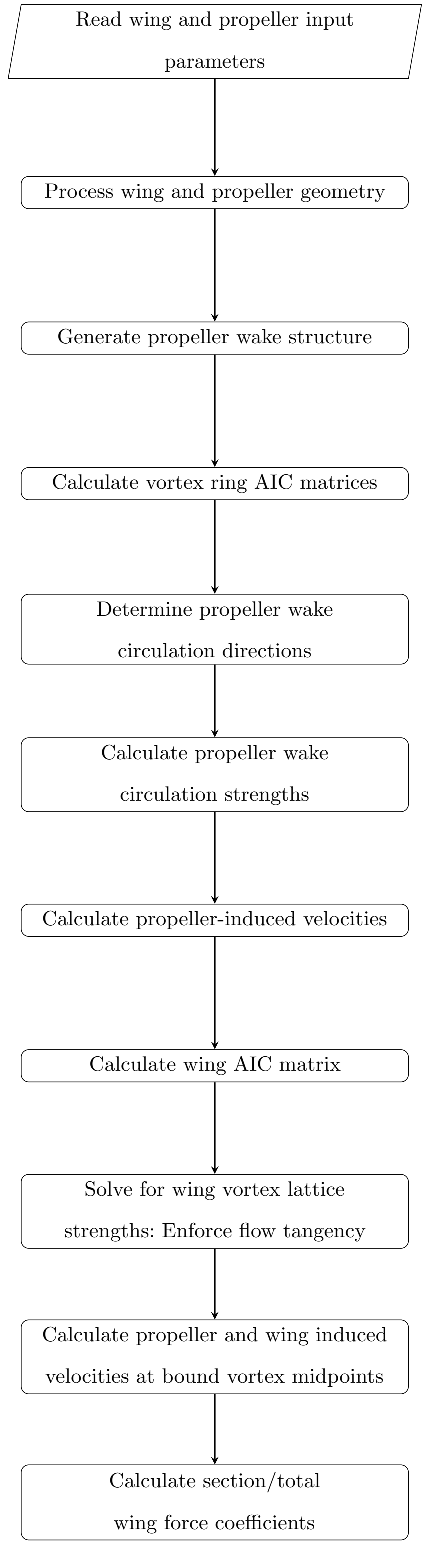

Figure 2.10: Propeller-wing interaction modeling procedure.

2.4 Model Capabilities and Limitations

A fundamental feature of the combined model is that the propeller wake effects and wing aerodynamics are calculated separately. This allows the user to toggle the propeller effects as desired, facilitating comparisons with clean wing configurations. In the combined model, a one-way interaction between the propeller and wing is assumed; that is, the propeller wake affects the wing aerodynamics, but not vice versa.

As described in section 2.1, the propeller wake model is intended for fast computations of the slipstream velocities and the resultant effects on immersed lifting surfaces. In the interest of computational performance, the wake is modeled using basic information for the propeller geometry and operating condition, including position, diameter, thrust coefficient, RPM, thrust direction, and rotation direction. Multiple propellers can be defined with different operating conditions. Specific blade information—such as chord, twist distributions and sectional aerodynamic properties—is not required to model the propeller vortex system. This increases the utility of the model for analysis cases where such blade data is not available. The simple relationship between the propeller inputs parameters enables quick generation of the propeller wake structure and corresponding aerodynamic influence coefficient matrices. These matrices are linearly scaled by the vortex strengths, which are estimated from the propeller operating conditions. With this information, solutions for the induced velocity are readily obtainable.

Limitations of the propeller wake model are also considered. The assumptions of a constant bound circulation along the blade and axial flight operation restrict the model to the analysis of propellers that are exactly or approximately uniformly-loaded. The model is also best suited for low-to-moderately loaded propellers. Static cases cannot strictly be handled since a forward velocity is currently required to generate the vortex ring distribution; however, such cases can be approximated by prescribing a small forward velocity. Furthermore, slipstream contraction is also neglected in this model. The effect of this assumption is evaluated in section 3.2.1 by comparing induced axial velocity distributions from the current model with corresponding data from a higher-order free-wake model that accounts for contraction [20].

Since the vortex rings are modeled with a uniform diameter and the bound vorticity is uniformly distributed across the propeller, there is no induction of a radial velocity component in the wake. The radial velocity is typically much smaller than the axial and tangential components, and its effect on the wing aerodynamics is not largely significant as long as the propeller axis is vertically aligned with the plane of the wing surface. The effect of the radial induced velocity is also confined to the contracting portion of the slipstream, which usually occupies a distance of less than 1 or 2 propeller diameters behind the disk for low-to-moderate values of the propeller loading [27].

The wing aerodynamic model contains the capabilities and limitations inherent in the Weissinger method. In the current implementation, horizontal and vertical lifting surfaces can be modeled as discrete patches with variable chord, zero-lift angle of attack and linear twist distributions. The patch leading edge coordinates are defined manually to allow for the incorporation of taper, sweep and dihedral. For each patch, a different number of panels can be specified to control the lattice density across the surface. The wing geometric angle of attack can be specified as a scalar or as a range of values to facilitate analysis at multiple conditions.

Due to the inviscid nature of the Weissinger method, viscous effects and related phenomena, such as stall, cannot be modeled without appropriate corrections. Another assumption of this method is that the chordwise bound vorticity of the wing can be concentrated into a single line along the quarter-chord point. As a result, each panel contains only a spanwise distribution of vorticity. This limits the applicability of the method to wings of moderate or high aspect ratio, where the relative effect of the chordwise vorticity distribution is small. Swept wings can also be modeled with sufficient accuracy, although numerical discretization errors can arise if the sweep angle is too large [28]. This modeling capability is validated in section 3.3.

2.4.1 Summary of Modeling Assumptions

To facilitate future work, this section presents key assumptions and summarizes their effects in the current model. Several of the assumptions allow for a simplified representation of the propeller-wing system to reduce computation time and permit fast aerodynamic modeling. The current work is therefore suited to analyze cases that can be approximated by the following conditions:

1. **The propeller-wing system operates in potential flow.** This limits the application of the model to inviscid analyses. As a result, viscous-related phenomena, such as boundary layer separation at high angles of attack, are not currently captured. To account for this, a separate viscous model or empirical correction could be applied.

2. **The propeller operates in axial flight.** In this case, the propeller axis is fixed to align with the freestream direction, regardless of the wing angle of attack. Predictions of the streamtube trajectory and induced loads on the wing are therefore less accurate when the wing operates at a higher angle of attack. There is also currently no provision to model advancing and retreating blade effects, which would generate an axisymmetric disk loading and produce a yawing moment on the aircraft.

3. **The propeller disk is uniformly loaded.** Under this condition, the distribution of bound vorticity over the disk is axisymmetric, and a time-averaged streamtube can be modeled according to the representation outlined in section 2.1. The assumption of a uniformly-loaded disk also entails a uniform inflow at the disk, which correlates with the previous assumption of an axial flight condition. To generalize the model for non-axial flight conditions, a non-uniform inflow distribution model would be required, along with modifications to the calculation of the streamtube trajectory.

4. **The bound circulation strength is constant along the blades.** For this reason, the trailing vortices emanate only from the blade tips. The trailing vorticity is therefore concentrated on the surface of the time-averaged cylindrical vortex sheet. By discretizing the tangential vorticity into axisymmetric vortex rings, the induced axial velocity distribution is nearly uniform along each streamtube cross section. This approximation may be improved by accounting for some spanwise variation in the bound circulation through modeling a concentric trailing vortex structure at an intermediate radial location along the blade.

5. **The hub vortex is concentrated into a line along the propeller axis.** This representation affects the distribution of the induced velocity, particularly in proximity to the propeller axis. By extension, the wing loading is slightly overestimated for panels immersed near center of the streamtube. To correct for this effect, the hub vortex may be modeled as a separate vortex mesh structure to account for its size. This could mitigate the effect of induced velocities that are currently overestimated.

6. **The propeller streamtube has a constant diameter.** In the absence of a contracting streamtube, there is no induction of radial velocity, and contraction effects in proximity to the disk are not captured. The relative effect of the slipstream contraction is evaluated by applying conservation of mass along the streamtube, between the propeller disk and a cross section far downstream. In this process, the far-field slipstream radius r_∞ is estimated as

$$r_\infty = R\sqrt{\frac{V_\infty + v_i}{V_\infty + 2v_i}} \tag{2.44}$$

where v_i is the induced velocity at the propeller disk, which is a function of the disk loading. By inspection, the radial contraction becomes less significant as $V_\infty/v_i \to \infty$, which corresponds to some combination of high advance ratio and low disk loading. To improve the prediction accuracy for more general cases, a prescribed slipstream contraction model could be added without significant computational expense.

7. **The propeller and wing operate with one-way coupling.** It is assumed that the propeller slipstream affects the wing aerodynamics, but the wing has no effect on the propeller loading or slipstream geometry. This simplification neglects any deformation of the propeller streamtube due to the induced flow field generated by the wing. A possible solution to enable two-way coupling is to iteratively compute the wing-induced loading on the propeller, determine perturbations to the streamtube geometry and recalculate the wing loading and vortex lattice strengths until a converged solution is obtained.

8. **The chordwise distribution of vorticity along the wing is negligible.** This is a primary assumption of the Weissinger method, which limits the accuracy of the model for wings with low aspect ratio. A more accurate prediction of the aerodynamics for low aspect ratio wings may be obtained with the incorporation of a vortex lattice method that accounts for both spanwise and chordwise distributions of the bound vorticity.

Chapter 3

Results

3.1 Parameter Convergence

The induced velocity solutions from the propeller wake model are sensitive to several discretization parameters over a certain range of values. These parameters include the number of vortex rings N_r, number of longitudinal filaments N_l and number of wake periods.

Through a series of test cases, the normalized ring spacing $\Delta x_r/R$ was identified as a characteristic parameter of the discrete vortex ring model (VRM). Figure 3.1 shows the effect of this spacing on the axial velocity distribution of an example propeller, which is normalized by the tip speed $V_{\text{tip}} = \omega R$. For reference, the velocity distributions are compared against an analytical solution for the axial velocity induced by a semi-infinite helical vortex of constant diameter [23]. It is observed that large values of ring spacing cause an oscillatory behavior in the axial velocity distribution, resulting from numerical discretization errors. As the spacing is decreased, the oscillations in the velocity are dampened until a converged solution is obtained for $\Delta x_r/R \approx 0.8$. This metric is useful in determining the minimum number of rings necessary to accurately model the induced axial velocity, which is typically the dominant component in the propeller slipstream. Further reductions in the ring spacing will produce slightly more refined solutions but with an increase in the required number of computations. This is not a problem since the current model is capable of quick computations even for a large number of vortex rings. As a conservative estimate, the following studies

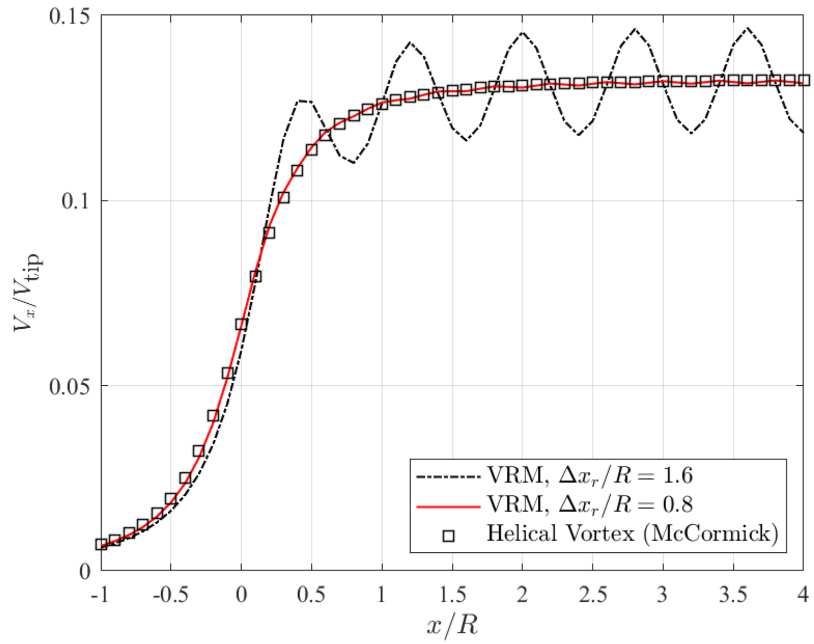

Figure 3.1: Axial distribution of centerline axial induced velocity for different values of normalized ring spacing $\Delta x_r/R$; $V_\infty = 20$ m/s, $N_b = 1$, $R = 0.5$ m, $C_T = 0.2$, $J = 0.4$.

employ a ring spacing $\Delta x_r/R < 0.75$ for a converged velocity distribution.

An appropriate number of downstream propeller revolutions should also be modeled to accurately resolve the axial velocity distribution in the far-wake. Combining the determined constraint on the ring spacing with equation 2.13, the total number of revolutions modeled should satisfy $N_{\text{rev}} < 0.8N_r/p$ for suitable results. A specific value is chosen to model the propeller wake effects far enough downstream for accurate velocity predictions at the longitudinal position of the wing.

Figure 3.2 illustrates the effect of the longitudinal filament spacing $\Delta\theta$ on the induced tangential velocity distribution in the wake. A non-dimensionalized form of the tangential velocity is compared with data from Branlard and Gaunaa [22], who constructed the complete flow field of a cylindrical vortex wake to model wind turbines with finite tip-speed ratios. For these comparisons, the wind turbine convention outlined in section 2.1.3 is used. The data is also generated for an inviscid case, such that the vortex core radius is zero. A converged solution is obtained as the spacing decreases, or as additional longitudinal filaments are modeled around the circumference of the slipstream. This is consistent with

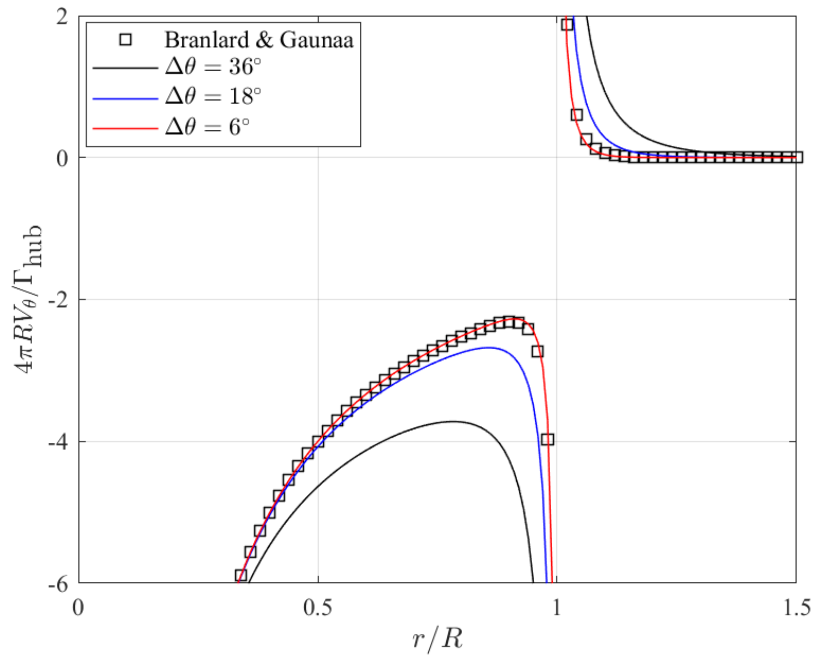

Figure 3.2: Radial variation of tangential velocity with variable longitudinal filament spacing $\Delta\theta$.

the time-averaging concept discussed in section 2.1. It is observed that $\Delta\theta = 6°$ provides good agreement with the analytical solution, indicating that the angular value should be kept approximately at or below this value for the tangential velocity calculation.

Figure 3.3 shows the bound vortex contribution to the tangential velocity in a wind turbine wake at variable axial locations downstream of the rotor plane. The influence of the bound vortices is greatest close behind the rotor plane. At the fixed axial locations depicted, the effect of the bound vortices decreases until it vanishes outside the wake boundary. As axial locations further downstream are considered, the bound vortices produce virtually zero tangential velocity inside or outside the slipstream. For the case shown, the bound vortex system is shown to have no effect beyond one propeller-diameter length downstream.

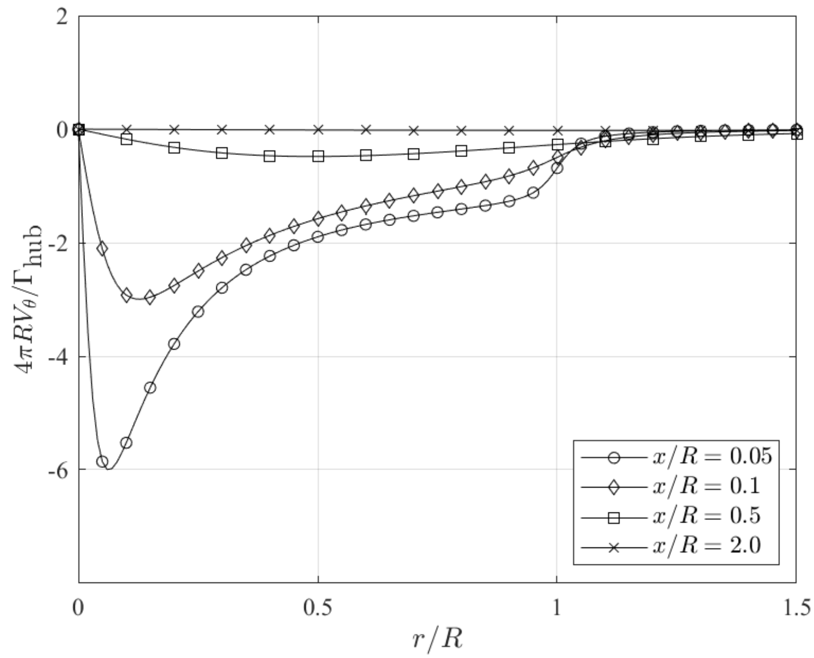

Figure 3.3: Radial distribution of tangential velocity induced by the bound vortices at different axial locations x/R.

3.2 Propeller Wake Model Validation

3.2.1 Axial Induced Velocity

A key assumption of the current model is that the propeller slipstream does not contract. The effects of this assumption are evaluated by comparing the induced axial velocity distribution against corresponding data produced from the implementation of a free-wake vortex ring model developed by Bontempo and Manna [20]. In the adapted approach, the propeller slipstream is represented by a series of axisymmetric vortex rings that converge into a semi-infinite vortex cylinder in the far wake. The vortex rings are modeled to convect with the local flow field, thereby accounting for wake contraction. A force-free condition is enforced along the edge of the slipstream to obtain the vortex ring strengths, and a kinematic constraint is imposed to ensure that the streamtube edge is aligned with the flow field. These two boundary conditions are iteratively applied until a converged wake solution is obtained.

Figure 3.4 compares the axial velocity distributions for a propeller with radius $R = 0.5$ m,

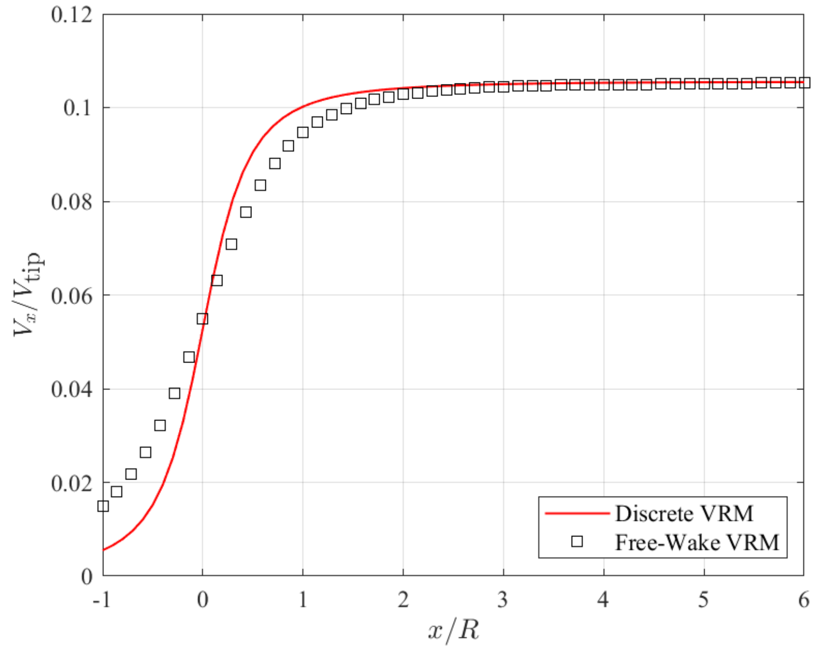

Figure 3.4: Axial variation of centerline axial induced velocity from discrete VRM with no contraction compared with a free-wake vortex ring model that predicts 9% slipstream contraction; $R = 0.5$ m, $C_T = 0.2$, $V_\infty = 20$ m/s, $J = 0.6$.

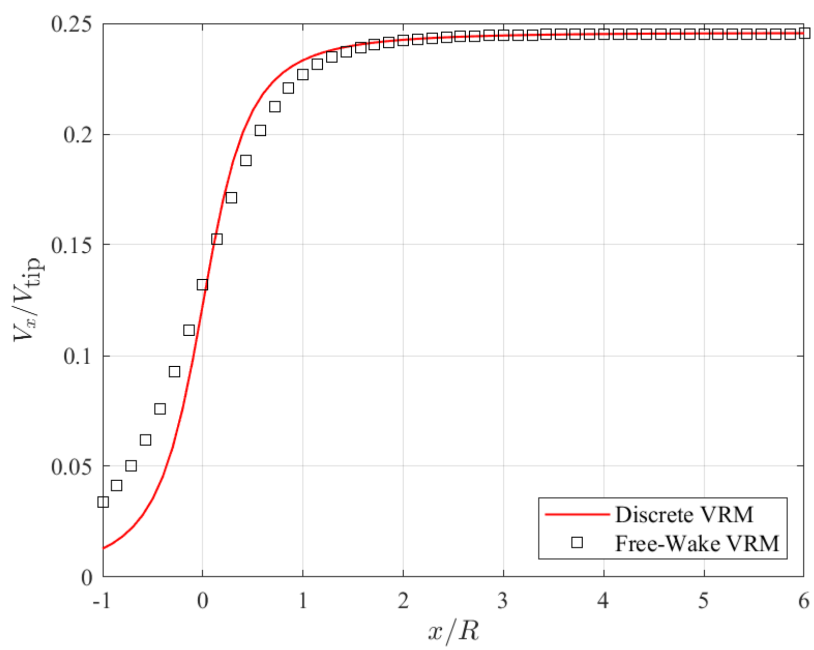

Figure 3.5: Axial variation of centerline axial induced velocity from discrete VRM with no contraction compared with a free-wake vortex ring model that predicts 15% slipstream contraction; $R = 0.5$ m, $C_T = 0.6$, $V_\infty = 20$ m/s, $J = 0.6$.

thrust coefficient $C_T = 0.2$, flight speed $V_\infty = 20$ m/s, and advance ratio $J = 0.6$. Using these parameters, the free-wake model predicts a 9% contraction of the wake. Figure 3.5 presents a similar case with a slightly higher thrust coefficient $C_T = 0.6$ and a predicted contraction of 15%. It is notable that the slipstream contraction effect increases at a higher thrust coefficient. This is due to the induction of a greater component of axial velocity when the propeller is highly-loaded. By the principle of continuity for incompressible flow, the total axial velocity and streamtube cross-sectional area follow an inverse relationship in order to conserve the mass flow rate along the wake. Thus, a higher induced axial velocity results in a greater reduction in the slipstream radius.

In general, the discrete vortex ring model compares well with the iterative free-wake model. Both methods predict a very similar value for the induced axial velocity at the propeller plane. The greatest discrepancy is observed within one propeller-diameter downstream, suggesting the effects of contraction are dominant in this region. In the far wake, both distributions converge to effectively the same axial velocity, which is approximately twice that at the propeller disk as predicted by classical momentum theory.

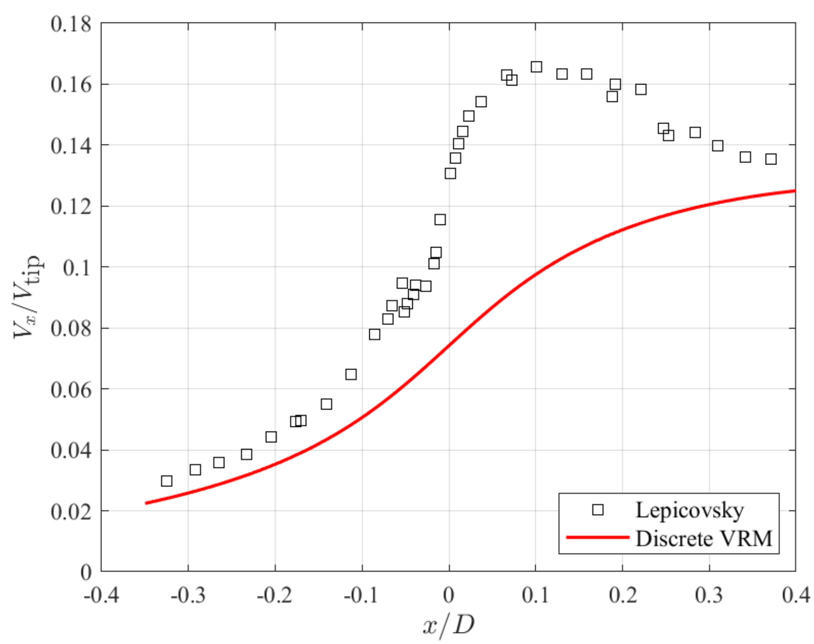

Figure 3.6: Axial velocity distribution in the slipstream; $N_b = 2$, $R = 0.1651$ m, $C_T = 0.1$, $V_\infty = 0$ m/s, RPM $= 4250$, $r/R = 0.693$.

In figure 3.6, the axial velocity distribution is compared with experimental flow field measurements of a 2-bladed, static propeller, collected by Lepicovsky [29] using laser velocimetry. It should be noted that the current model cannot handle a strictly static propeller case, so a small forward velocity component was prescribed while keeping the advance ratio below the order of 10^{-4}. As shown, the vortex ring model is capable of capturing the velocity profile upstream of the propeller. It gives an under prediction of the measured flow velocities but follows a similar trend in the growth of the axial velocity along the slipstream. The measured axial velocity increases significantly across the propeller plane, peaking at around $x/D = 0.1$ before decreasing slightly and approaching a nearly constant value. This effect is not captured by the vortex rings, whose combined influence results in a monotonically increasing velocity distribution. As a result, the predicted downstream velocity is about 8% lower than the corresponding experimental value.

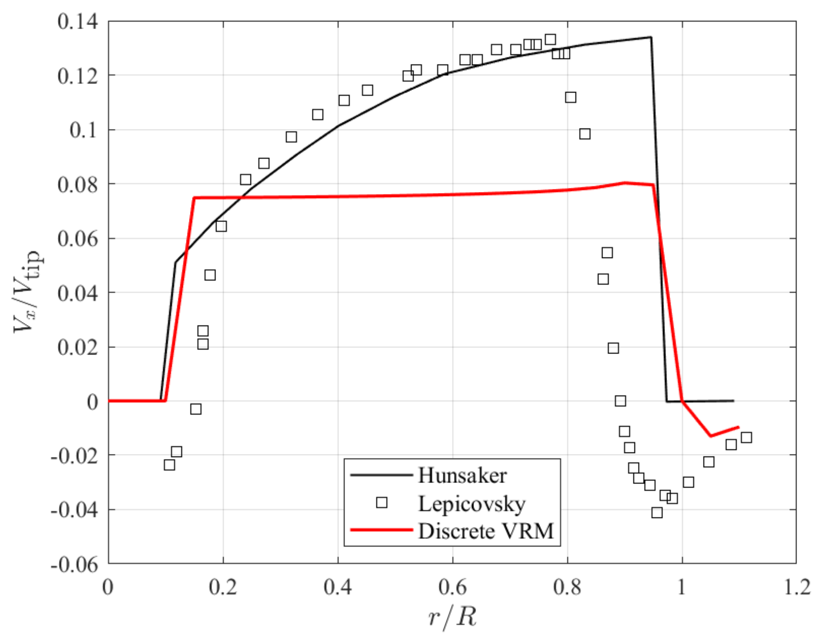

Figure 3.7: Radial variation of axial induced velocity in the slipstream; $N_b = 2$, $R = 0.1651$ m, $C_T = 0.1$, $V_\infty = 0$ m/s, RPM = 4250, $x/D = 0.009$.

In figure 3.7, the radial distribution of axial velocity in the slipstream is compared against the Lepicovsky data, as well as a numerical vortex lattice method prediction by Hunsaker

[30]. The hub radius was estimated at 10% for applying a velocity cutoff since the associated geometric information was not provided in the experimental work. Whereas the experimental and numerical data exhibit an increasing axial velocity moving towards the edge of the slipstream, the vortex ring model predicts a nearly constant axial velocity distribution. The velocity magnitude is under-predicted by the vortex ring model over a large radial distance and attains a value that is approximately half of the peak velocity attained in the other distributions. This discrepancy is likely due to the lack of a modeled spanwise variation in the circulation along the blade, along with the circumferential concentration of the tangential vorticity in the axisymmetric vortex rings. Outside of the wake, the rings induce a small axial velocity component in the upstream direction, which appears to approach the value predicted by the experimental data. Based on these observations, the vortex ring model performs reasonably well when taking into account the simplifying assumptions.

3.2.2 Tangential Induced Velocity

The tangential velocity induced by the propeller primarily alters the angle of attack distribution along the wing. As such, accurate calculations of this velocity component are critical to effectively model propeller-wing interaction. Figures 3.8, 3.9 and 3.10 compare the tangential velocity distributions from the tip, hub and bound vortices with corresponding analytical data from the work of Branlard and Gaunaa described in section 3.1. In each case, predictions from the discretized cylindrical wake model match well with the analytical model. The contribution from the tip vortices is observed to approach infinity on either side of the wake boundary due to the absence of a viscous core model. As seen in figure 3.9, similar behavior is exhibited by the hub vortex when moving closer to the rotor center. Figure 3.10 illustrates the tangential velocity induced along the radial direction by the bound vortices. The influence of the bound vortex system decreases when approaching the slipstream edge and vanishes at radial positions outside of the slipstream. The total tangential velocity is obtained as a superposition of the three contributions, which is shown in figure 3.11. It can be seen that the total tangential velocity vanishes further outside the slipstream and contains singularities in the interior due to the root and tip vortices. As described in section

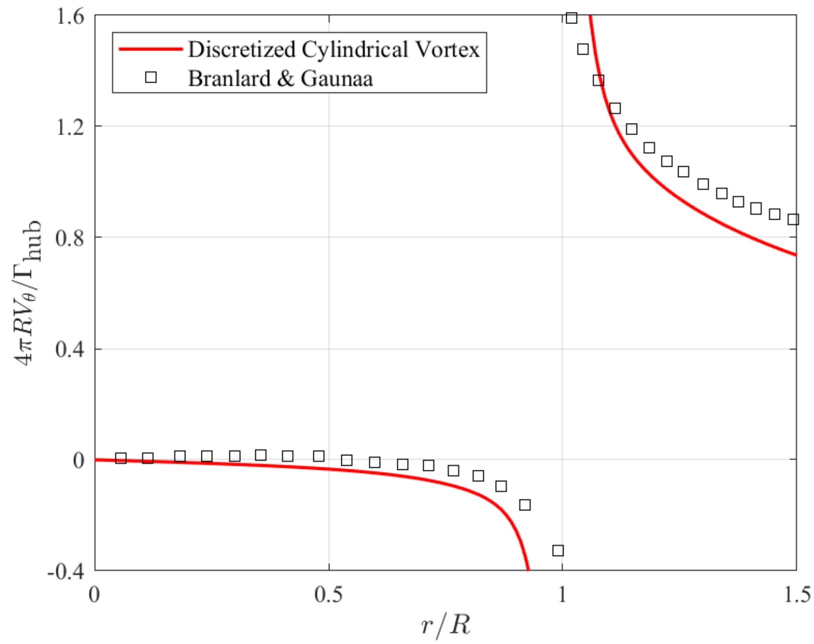

Figure 3.8: Radial distribution of tangential velocity induced by the tip vortices at $x/R = 0.1$.

2.1.1, the current model is capable of handling these singularities through the prescription of a vortex core radius, which applies a smoothing function to the induced velocities to simulate viscous effects in proximity to the cores.

3.3 Wing Model Validation

The current implementation of the Weissinger method is validated against data from several numerical and experimental works. This process is important for evaluating the behavior of the wing aerodynamic model as applied to various planform geometries and flight conditions. In the following analyses, the wing planform is discretized into $N_p = 100$ panels.

3.3.1 Spanwise Lift Distribution

Figure 3.12 compares the calculated lift distributions with experimental data from Stüper [31] for a rectangular wing of aspect ratio $\text{Æ} = 4$ with a Göttingen 409 airfoil section and circular end caps of diameter 0.32 m. In this validation work, the end caps are approximated as vertical square panels with diagonal length equal to the end cap diameter. Numerical

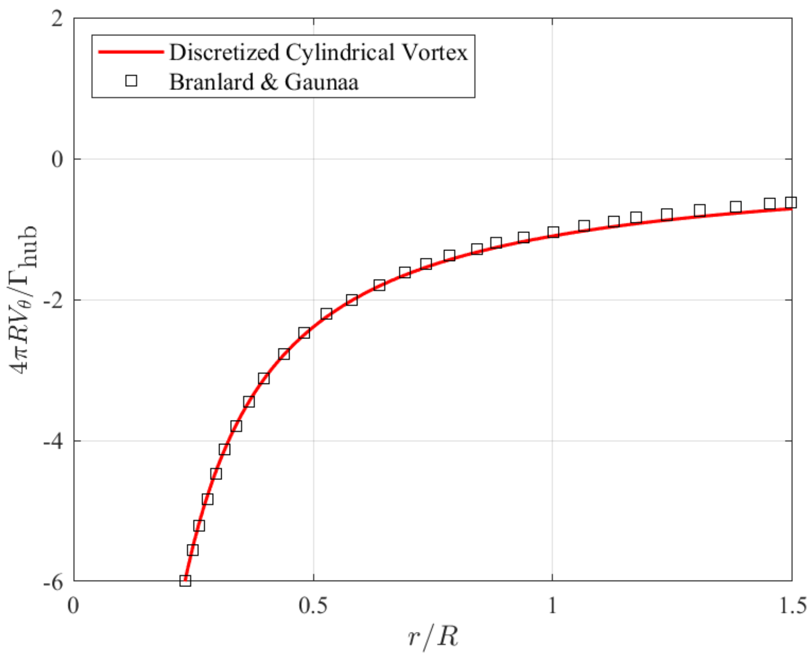

Figure 3.9: Radial distribution of tangential velocity induced by the hub vortex at $x/R = 0.1$.

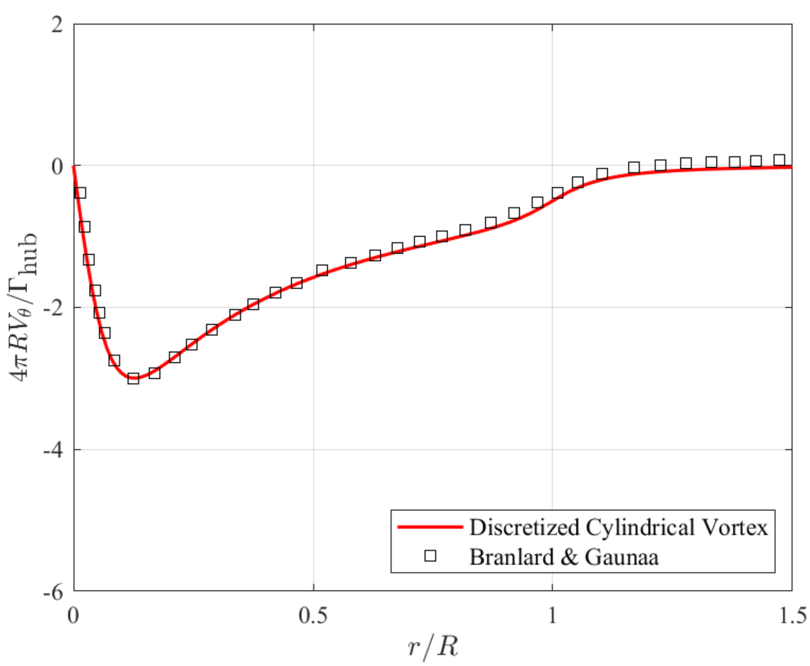

Figure 3.10: Radial distribution of tangential velocity induced by the bound vortices at $x/R = 0.1$.

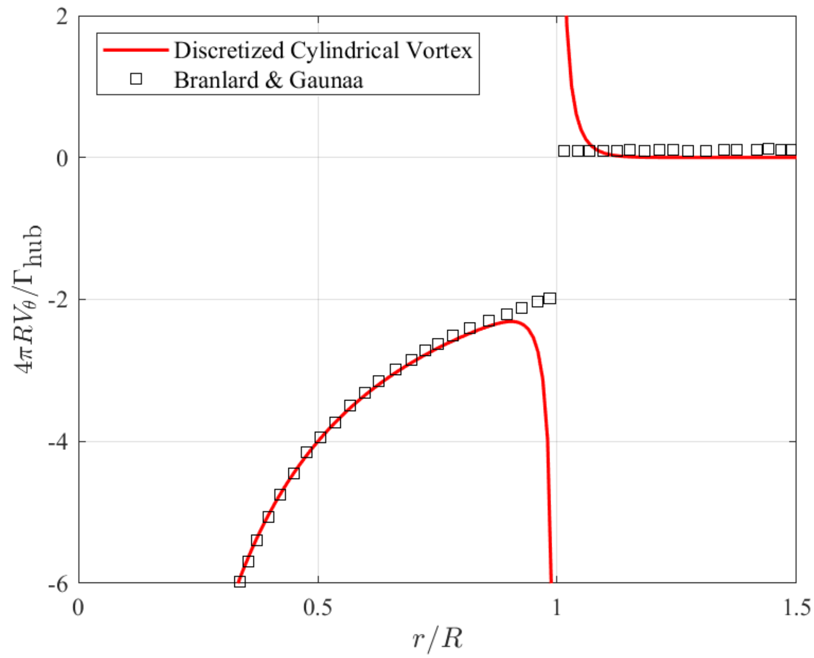

Figure 3.11: Radial distribution of tangential velocity induced by the total vortex system at $x/R = 0.1$.

solutions from a 3D lifting line approach by Hunsaker [30] are also included for comparison. Results from the Weissinger method agree well with both the numerical and experimental data at $\alpha = 4°$ and $\alpha = 8°$, giving only a slight over-prediction in each case. At $\alpha = 12°$, the Weissinger method predicts a similar distribution shape but significantly overestimates the lift coefficient magnitude. Unlike the numerical method employed by Hunsaker, which incorporates semi-empirical viscous corrections to the airfoil section lift and drag, the Weissinger method is purely inviscid and does not account for the significant reduction in lift caused by boundary layer separation and stall that are likely to occur at higher angles of attack. Small differences may also be caused by approximating the circular end caps as square panels, thereby altering the flow near the wing tips. Furthermore, considering the relatively low aspect ratio $Æ = 4$ of the wing, it is possible that the assumption of the Weissinger method to neglect the chordwise vorticity is not completely valid for this geometry. However, any such discrepancies appear to be marginal, particularly at lower angles of attack.

The Weissinger method is also compared against a higher-fidelity Reynolds-Averaged

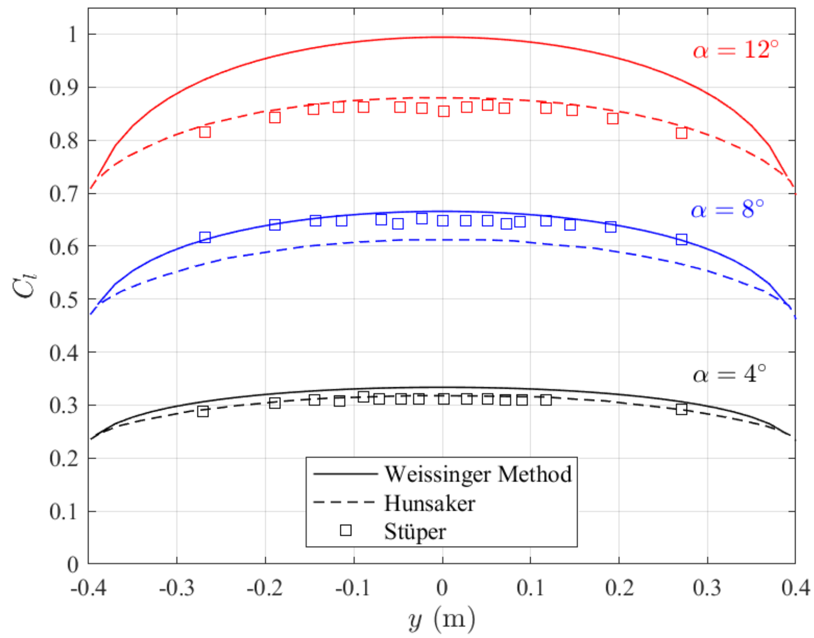

Figure 3.12: Lift coefficient distribution of a rectangular wing with Göttingen 409 airfoil sections and circular end caps; $b = 0.8$ m, $c = 0.2$ m, $V_\infty = 30$ m/s.

Navier Stokes (RANS) CFD solution obtained by Seo, et. al. [32] for the lift distribution of a rectangular wing with aspect ratio $AR = 8.8$ and a symmetric NACA 0012 airfoil section. The CFD solution was obtained using a compressible flow solver with viscous effects and included a modified Spalart-Allmaras turbulence model. In figure 3.13, the semi-span lift distribution from the Weissinger method is compared with the CFD result, showing reasonable agreement between both predictions. The greatest discrepancy is observed at the wing root and along the inboard region, which, as indicated previously, may arise in part from the lack of a viscous model in the Weissinger method. The distributions show greater agreement moving towards the wing tip and coincide at a location near 85% of the half-span.

3.3.2 Wing Lift Coefficient

The calculation of the total wing lift coefficient is validated with data obtained from an experimental work of Veldhuis [33]. This study involved low-speed wind tunnel testing of a propeller-wing configuration, referenced as PROWIM ("propeller wing interference model"),

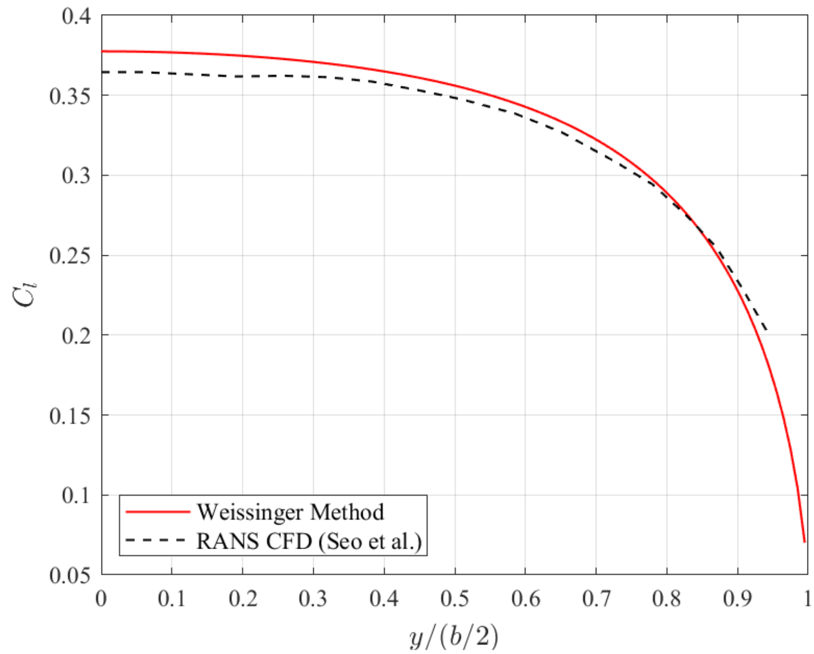

Figure 3.13: Lift coefficient distribution along the semi-span of a rectangular wing with NACA 0012 airfoil sections; $b/2 = 5.7$ m, $c = 1.295$ m, $V_\infty = 30.13$ m/s, $\alpha = 4°$.

which used a constant-chord half-span with full-wing aspect ratio $\mathcal{R} = 5.33$ and a symmetric NACA 64-A015 airfoil section. The wing contained a small rounded segment at the tip of the leading edge; however, its planform was approximated as a rectangle for validation purposes. An axisymmetric nacelle was mounted to the wing at a distance of 0.3 m from the root, and a reflection plate was positioned at the wing root to simulate the image of the full wing. The lift curve of the wing configuration with the propeller off is compared against the corresponding Weissinger method prediction in figure 3.14.

The lift curves exhibit excellent agreement up to about $\alpha = 6°$. At higher angles of attack, a noticeable reduction in the experimental lift curve slope is observed; the experimental data gives an average lift-curve slope $C_{L_\alpha} = 0.067$/deg compared to an average $C_{L_\alpha} = 0.071$/deg predicted by the Weissinger method across a 10° angle of attack range. This difference can be attributed to several factors, including the presence of viscous effects and interference effects from the wind tunnel that are not captured in the low-order model. Also, the presence of the nacelle generates a small axial velocity component in the wake [33], and, along with the propeller, introduces unaccounted effects in the flow field despite the propeller being off. Still, the numerical predictions of the lift coefficient magnitude are comparable over a considerable range of the operating angle of attack.

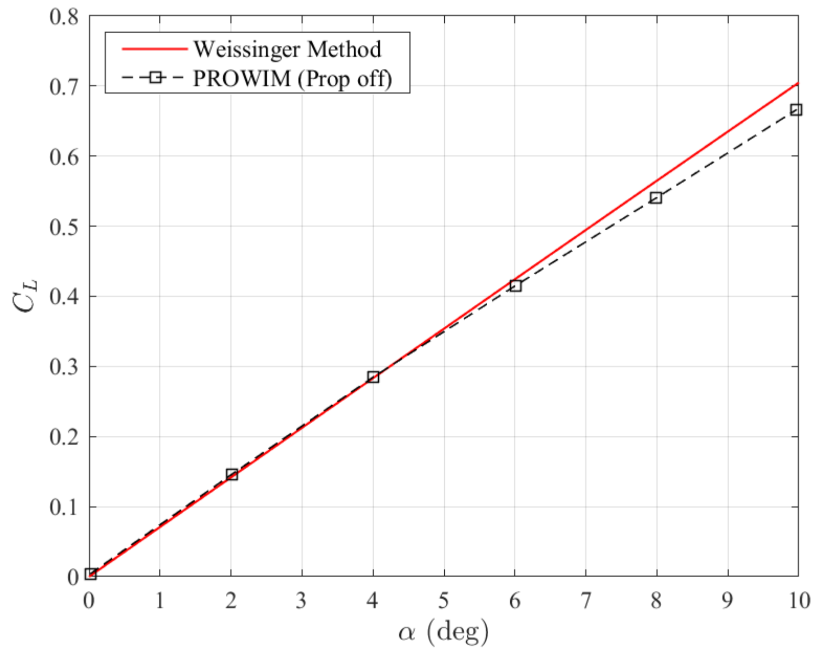

Figure 3.14: Lift curve for the PROWIM wing with propeller off; $b/2 = 0.64$ m, $c = 0.24$ m, $V_\infty = 50$ m/s.

Finally, the Weissinger method is validated against experimental data from Hunton [34] for a swept wing-fuselage combination installed in a 7 ft $\times$ 10 ft wind tunnel. In this study, the wing consisted of symmetric, untwisted NACA 64A010 airfoil sections, with a planform of aspect ratio $Æ = 6$, leading edge sweep $\Lambda_{\mathrm{LE}} = 45°$, root chord $c_r = 2.44$ m, and taper ratio $\lambda = 0.5$. Figure 3.15 compares the numerical and experimental lift curves. At all angles of attack, the Weissinger method overestimates the experimental lift coefficient, though decent agreement is observed in the linear C_L-α region. At $\alpha = 12°$, the numerical prediction of C_L is 7.6% greater than the experimental value. Beyond this angle of attack, the discrepancy grows significantly as the experimental curve departs from the linear aerodynamic regime due to the onset of flow separation. Additionally, the relatively low aspect ratio of the wing, combined with the significant sweep angle of 45°, likely contributes to notable differences in the lift calculation. In this case, the bound vortices are aligned

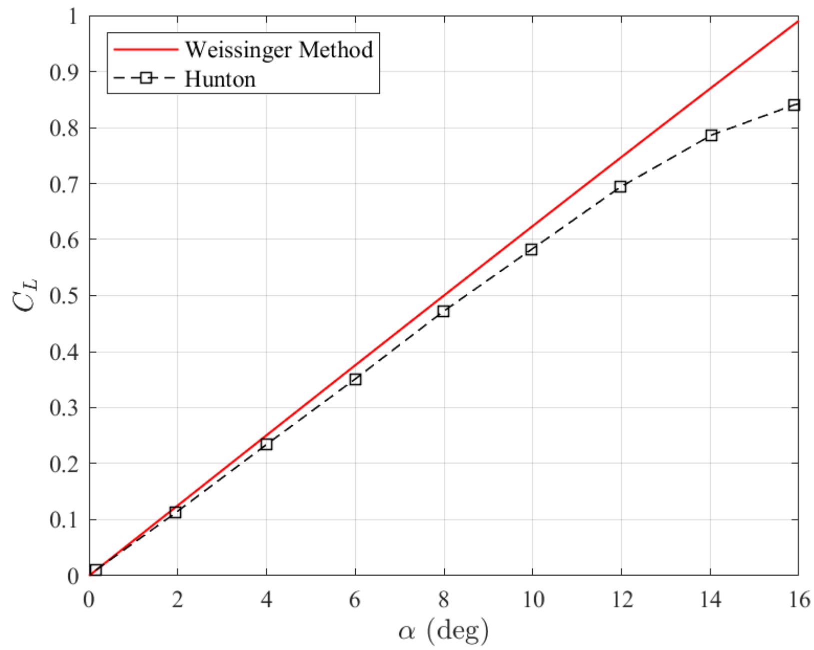

Figure 3.15: Lift curve for a swept and tapered wing with NACA 64A010 airfoil sections; $b = 10.97$ m, $c_r = 2.44$ m, $\lambda = 0.5$, $\Lambda_{\mathrm{LE}} = 45°$, $V_\infty = 65$ m/s.

equally in the streamwise and spanwise directions, resulting in a variation in the chordwise vorticity, along with a non-trivial component of spanwise flow along the wing. Furthermore, the presence of a fuselage body in the experiment alters the flow field, generating boundary layer interaction and interference that cause a local decrease in lift near the wing root. Nonetheless, the numerical method gives adequate predictions at low to moderate angles of attack despite neglecting these higher-order effects.

As demonstrated in this section, the current implementation of the Weissinger method provides a reliable calculation of the wing aerodynamics and performs well for various planform geometries and operating conditions within its limitations.

3.4 Combined Model Validation

The combined model incorporates propeller-induced velocities into the Weissinger method to calculate the modified wing loading. To investigate the localized and aggregate effects of propeller-wing interaction, predictions of the spanwise loading distributions and total wing loading for various configurations are presented in the following sections.

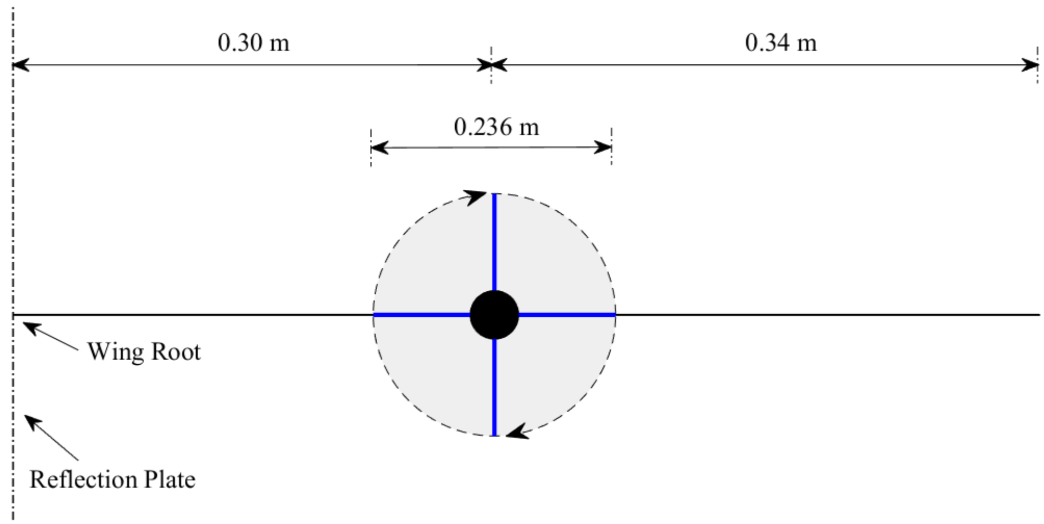

Figure 3.16: PROWIM propeller-wing configuration with inboard-up propeller rotation.

3.4.1 Spanwise Lift Distribution

Predictions of the lift coefficient distribution from the combined model are compared against numerical (VLM) and experimental data produced by Veldhuis [35] from the PROWIM study cited in the previous section. An aft view of the experimental propeller-wing configuration is shown in figure 3.16. The propeller was positioned 0.2618 m ahead of the wing quarter-chord line and operated with inboard-up rotation. Additionally, the blade root cutout was approximated as 29% of the propeller radius. The presence of the reflection plate is simulated in this work by modeling the full wingspan and defining an identical propeller with opposite rotation at a spanwise location symmetrically about the wing root. Veldhuis conducted tests with the wing at $\alpha = 0°$ and $\alpha = 4°$; results for each case are presented alongside the combined model predictions in figures 3.17 and 3.18, respectively. For reference, clean-wing lift distributions generated from the Weissinger method are also included to evaluate the overall effect of the propeller influence.

Since the wing employs an untwisted, symmetric airfoil, each section produces zero lift at $\alpha = 0°$ without the propeller, as predicted by the Weissinger method in figure 3.17. When accounting for the inboard-up propeller rotation, the Veldhuis VLM and experimental data exhibit a nearly symmetrical C_l distribution, with increased lift in the region of upwash near the root, decreased lift in the region of downwash, and vanishing incremental effects at

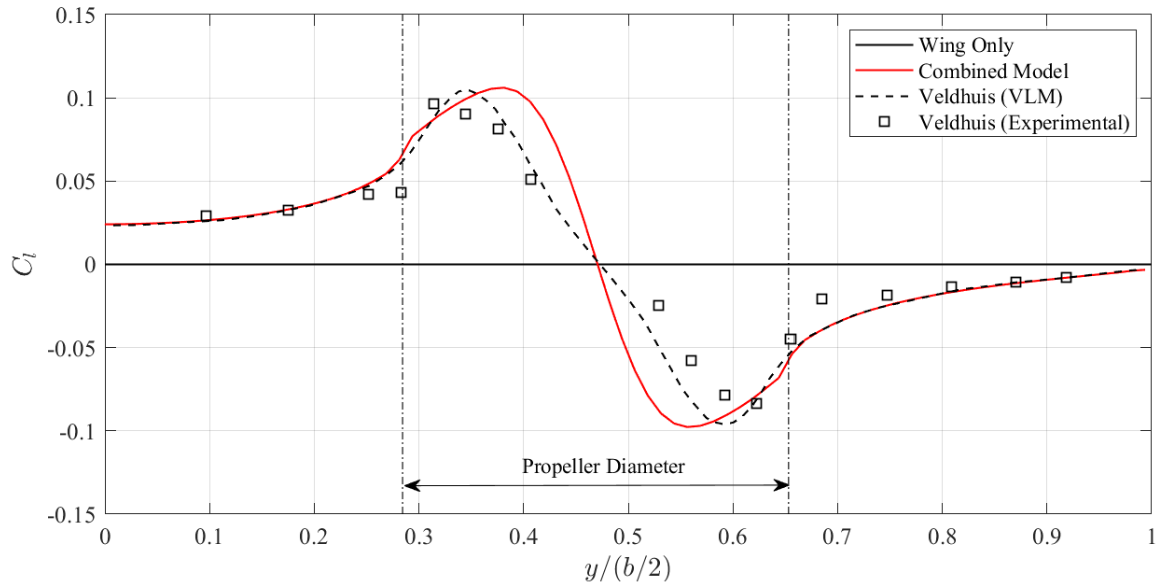

Figure 3.17: Spanwise lift distribution for the PROWIM wing with inboard-up propeller rotation; $b/2 = 0.64$ m, $c = 0.24$ m, $N_b = 4$, $R = 0.118$ m, $C_T = 0.1268$, $J = 0.85$, $\alpha = 0°$.

the wingtips. The combined model yields a distribution that agrees notably well with the Veldhuis data outside the propeller slipstream. Within the slipstream, similar values for the minimum and maximum lift coefficient are obtained. However, the model predicts a profile whereby the peaks are located closer to the propeller centerline, resulting in a steeper C_l variation across the hub region. The observed behavior arises from treating the hub as a single point in the plane of the propeller. As a result, the hub circulation is concentrated into a single line vortex along the propeller axis, rather than being distributed over the circumferential extent of the hub. By omitting the radial dimension of the hub, the model also does not account for an associated negative induced axial velocity component. This produces a small overestimation of the total velocity magnitude and loading distributions along wing panels in proximity to the propeller axis. The Veldhuis VLM model mitigates this effect by using a swirl recovery factor to prevent unrealistic velocities in the slipstream.

Figure 3.18 compares the C_l distributions with the PROWIM wing operating at an angle of attack $\alpha = 4°$. In this case, the effect of the propeller slipstream produces a similar trend in the spanwise lift distribution to that at the $\alpha = 0°$ condition. The propeller-on distributions indicate improved performance near the wing root in the region of upwash

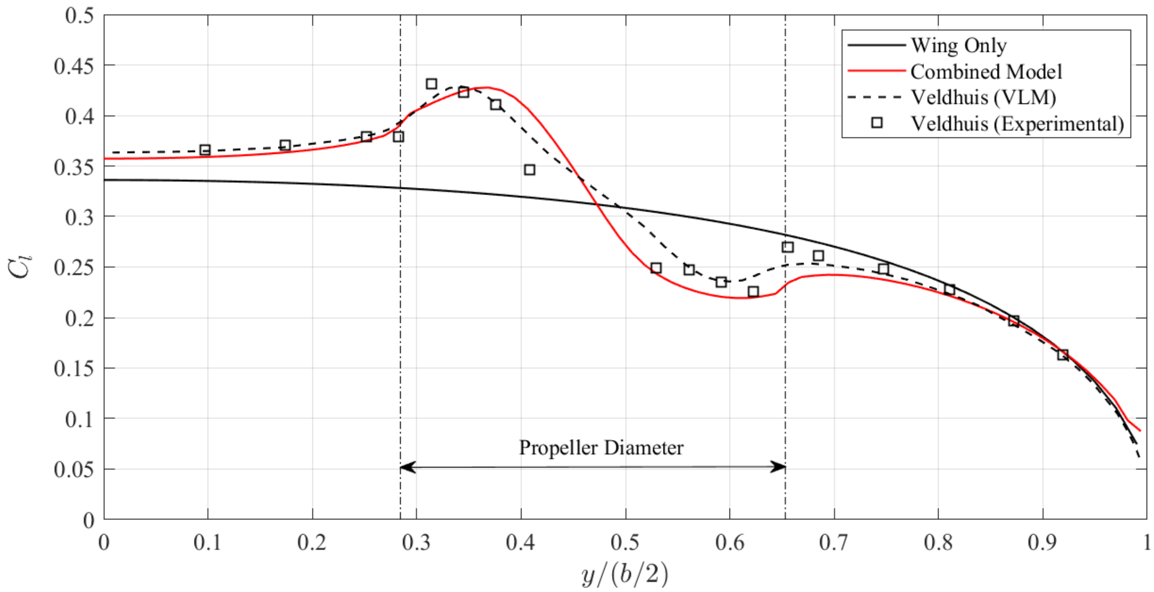

Figure 3.18: Spanwise lift distribution for the PROWIM wing with inboard-up propeller rotation; $b/2 = 0.64$ m, $c = 0.24$ m, $N_b = 4$, $R = 0.118$ m, $C_T = 0.1268$, $J = 0.85$, $\alpha = 4°$.

compared to the clean wing. Like before, the combined model performs well outside of the slipstream and reasonably predicts the C_l variation inside, showing similar discrepancies as in the $\alpha = 0°$ case due to the hub effects. It is likely that the loading in the downwash region is underestimated in part due to the near-constant distribution of axial velocity generated by the vortex rings along the slipstream radius. As seen from the validation data in figure 3.7, the vortex ring model under-predicts the axial velocity near the edge of the slipstream. The absence of a radial wake contraction model is also a possible factor.

At the outboard edge of the slipstream, the experimental data shows a sharp local increase in the section lift, which is only partially captured by the combined model. The localized difference in behavior across the slipstream edge may be caused by the viscous core model that is currently employed for the vortex rings. This core model applies a smoothing effect to the velocity distribution based on the perpendicular distance from the core of a vortex filament, as described in section 2.1.1. In the current implementation, the perpendicular distance is calculated to the point at which a vortex ring intersects the wing. Consequently, the core model provides an approximate calculation that does not incorporate the curvature of the vortex rings. This entails that the small negative axial velocity induced by the rings outside the slipstream is being overestimated in the current model. The existing calculation can potentially be improved by discretizing the rings into finite-length segments and applying the core model to each element. An inherent drawback of this approach is the increased computational cost resulting from the repeated calculations for all vortex segments.

3.4.2 Total Lift Coefficient

In this section, the combined model is evaluated for its ability to capture the overall effect of the propeller slipstream on the wing lift. Figure 3.19 shows the lift curves of the PROWIM wing [35] for each propeller rotation direction. In both cases, the combined model results follow closely with the Veldhuis data, generating similar lift-curve slopes. It should be noted that in the PROWIM study, the propeller nacelle was mounted to the wing and therefore operated at the wing geometric angle of attack. Since the combined model does not account for this change in propeller angle of attack, the thrust direction and slipstream orientation relative to the wing is slightly offset from the test condition. This offset modifies the angles of the velocity components relative to the wing. At low angles of attack, this difference in velocity is negligible by the small angle approximation. For larger angles of attack, a greater discrepancy in wing loading is observed; however, the current differences between the predicted and experimental lift coefficient values are still reasonably small. Furthermore, the combined model favorably captures the improvement in the total wing lift from the propeller slipstream effect.

The inboard-up rotation yields a slightly increased C_L benefit compared to outboard-up rotation at a given angle of attack. The additional incremental lift from the inboard-up rotation arises due to the action of the propeller upwash on the inboard panels, where the local lift coefficient is greatest. By reducing the downwash generated from the wing vortex lattice system in this region, the propeller upwash also creates a positive spanwise C_l gradient, which increases the section lift outside the slipstream, on the inboard side. Additionally, by symmetry, the propeller located on the other half of the wing also generates an induced upwash that further increases the local lift across the inboard region.

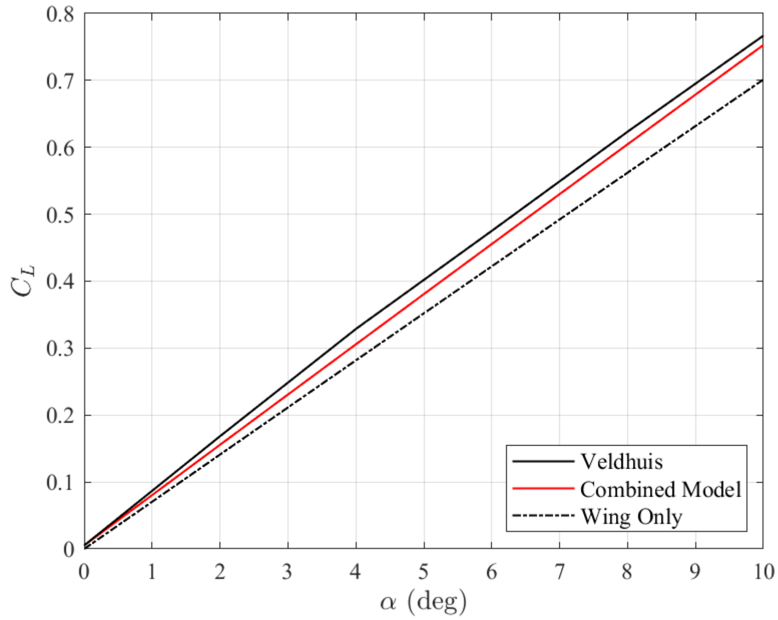

(a) Inboard-up rotation

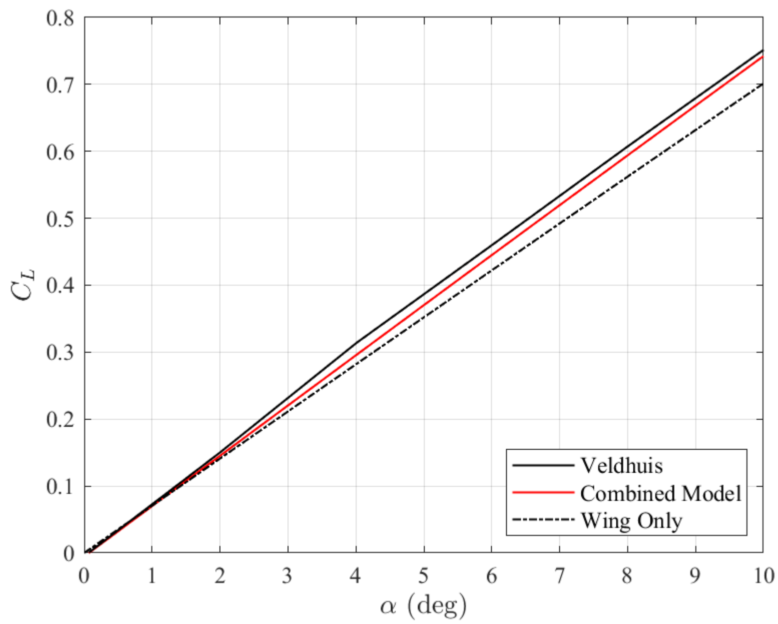

(b) Outboard-up rotation

Figure 3.19: Effect of propeller rotation direction on the PROWIM wing lift curve; $b/2 = 0.64$ m, $c = 0.24$ m, $N_b = 4$, $R = 0.118$ m, $C_T = 0.1268$, $J = 0.85$.

The outboard-up rotation produces a similar effect, although in this case, the upwash is generated in an outboard region, where the local lift is lower than that near the wing root. Furthermore, the propellers on either side of the full wing combine to increase the downwash at the inboard sections. This, however, is counteracted by the increased C_l in the propeller upwash region. By integrating the propeller influence on the lift distribution over the entire span, the outboard-up rotation still yields improved lifting performance, albeit smaller than for inboard-up rotation, over the corresponding clean-wing configuration.

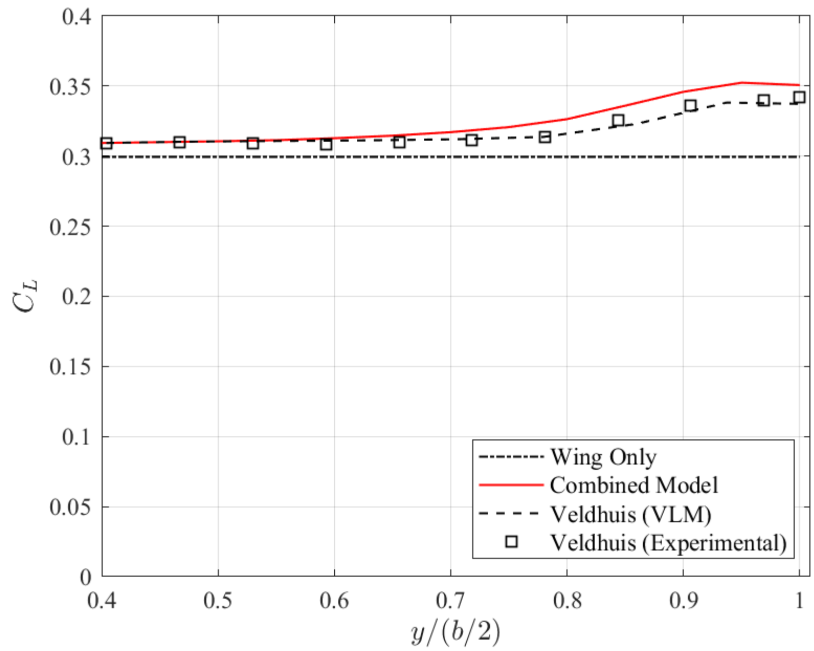

Figure 3.20: Variation of the APROPOS wing lift coefficient with propeller spanwise position for inboard-up rotation; $b/2 = 0.64$ m, $c = 0.24$ m, $N_b = 4$, $R = 0.118$ m, $C_T = 0.1268$, $J = 0.92$, $\alpha = 4.2°$.

The effect of propeller spanwise position on the total wing lift is also investigated. Figure 3.20 shows the wing lift coefficient as a function of the propeller position along the half-span for the APROPOS experimental setup used by Veldhuis [35]. The APROPOS setup utilized the same propeller geometry from the PROWIM study but with the nacelle detached from the wing and supported by a traversing strut. For testing, the propeller and wing operated at angles of attack of 0° and 4.2°, respectively. The propeller rotation direction was inboard-up, and the vertical position of the propeller was also kept constant throughout this study.

The predicted variation of lift matches well with the VLM and experimental data for inboard propeller positions up to about 50% of the half-span. Moving further towards the tip, the combined model overestimates the C_L by a small margin, producing values with a nearly-constant offset from the PROWIM results on the order of about 0.01. As discussed previously, this difference may be caused by the overestimation of the section lift near the slipstream center due to the absence of a dimensional hub model. Despite the offset, the combined model effectively captures the improved lifting performance exhibited by the PROWIM results as the propeller moves outboard. When positioned near the tip, the inboard-up rotating propeller generates an upwash at the outboard wing panels, reducing the influence of the tip vortex and increasing the effective aspect ratio of the wing. At these locations, the numerical models predict a slight tapering of the lift coefficient, which is not shown in the experimental data. This behavior may be caused by approximating the small curved segment at the wingtip as a rectangular edge. It is also possible that the tapering effect is caused as portions of the slipstream move laterally beyond the wingtip, a notion which is further discussed in section 3.4.5.

3.4.3 Distributed Propulsion

An important feature of the combined propeller-wing model is its ability to handle the aerodynamic effects of multiple propellers, which is critical for the design and analysis of distributed propulsion systems. For this purpose, the combined model is applied to a multi-propeller configuration from the work of Seo et al. [32]. This study analyzed the performance of several distributed propulsion setups using the numerical approach previously described in section 3.3.1, combined with the actuator disk method and blade element theory. For the current work, two test cases from the study were chosen for comparison. Both consisted of three identical propellers, equally spaced along the half-span of a rectangular wing. In the first "co-rotating" case, each propeller operated with inboard-up rotation, as shown in figure 3.21. For the second "counter-rotating" case, the center propeller operated with outboard-up rotation instead, as illustrated in figure 3.23.

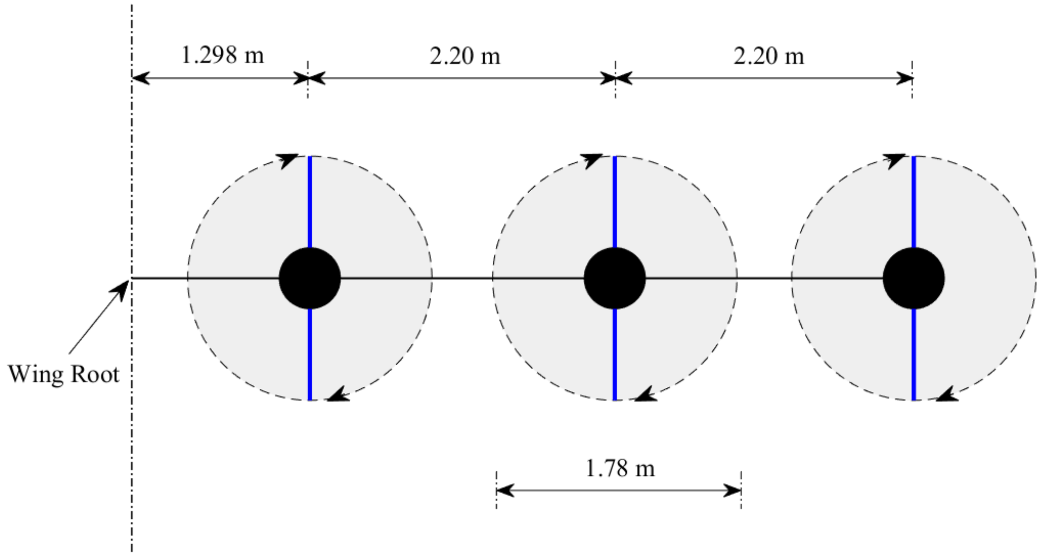

Figure 3.21: Half-span of the Seo wing with a co-rotating propeller configuration.

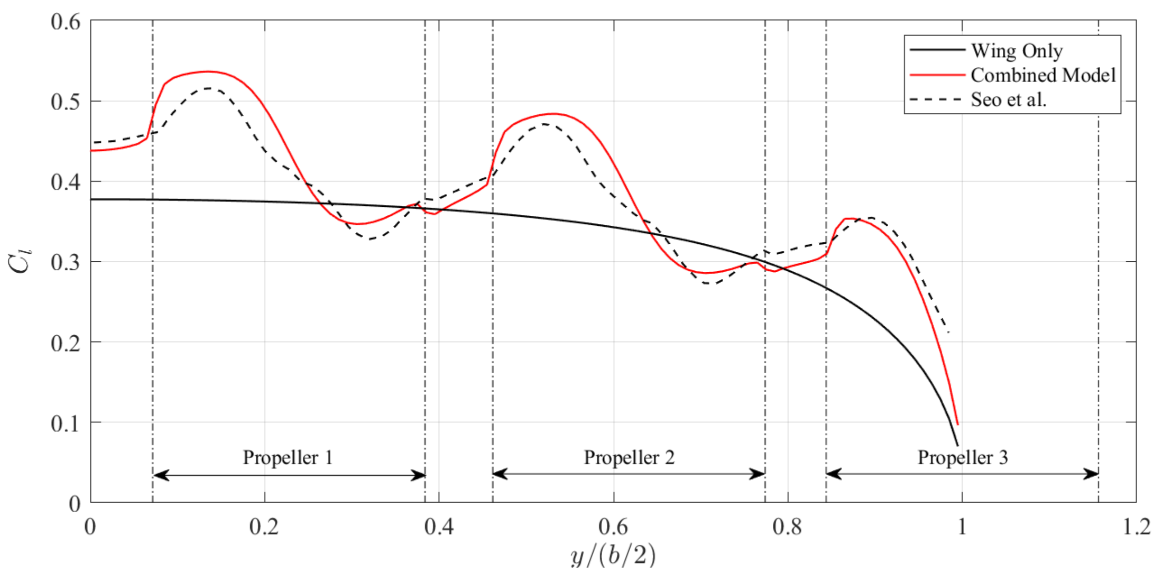

Figure 3.22: Spanwise lift distribution for the Seo with 3 co-rotating propellers on the half-span; $b/2 = 5.7$ m, $c = 1.295$ m, $N_b = 2$, $R = 0.89$ m, $C_T = 0.0766$, $J = 0.755$, $V_\infty = 30.13$ m/s, $\alpha = 4°$.

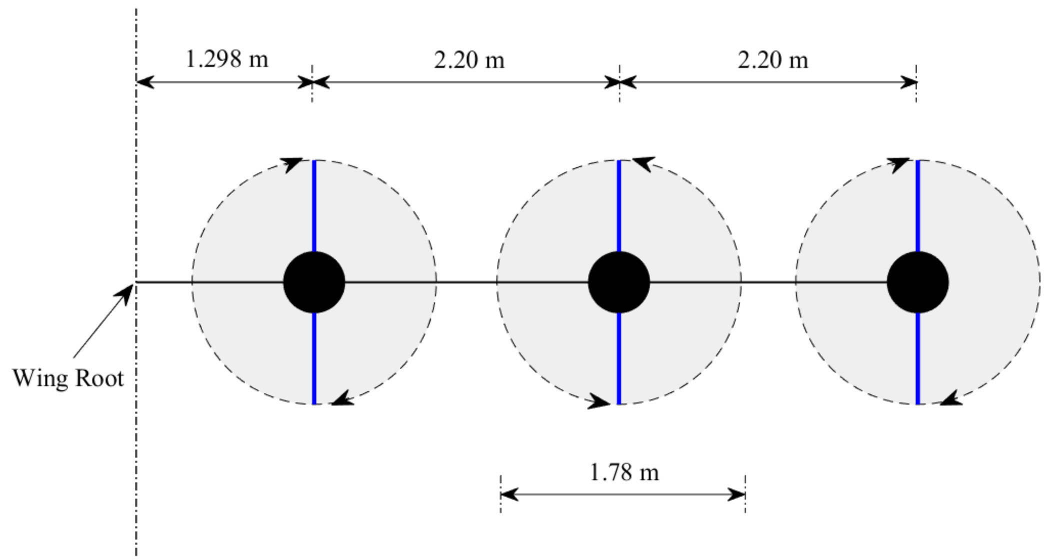

Figure 3.23: Half-span of the Seo wing with a counter-rotating propeller configuration.

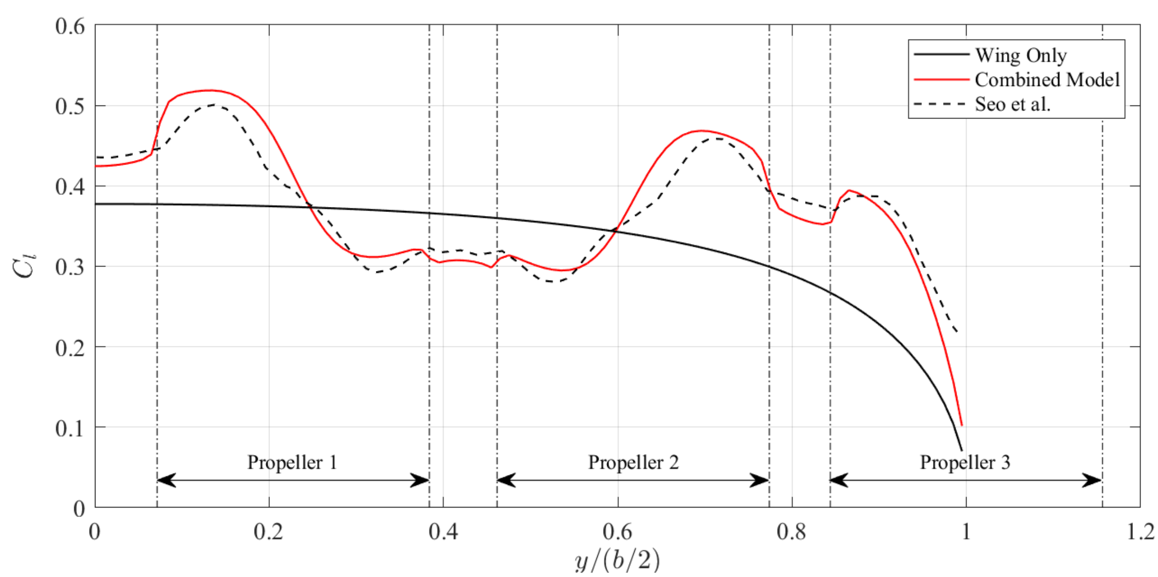

Figure 3.24: Spanwise lift distribution for the Seo wing with 3 counter-rotating propellers on the half-span; $b/2 = 5.7$ m, $c = 1.295$ m, $N_b = 2$, $R = 0.89$ m, $C_T = 0.0766$, $J = 0.755$, $V_\infty = 30.13$ m/s, $\alpha = 4°$.

A comparison of the lift distributions for the co-rotating case is presented in figure 3.22. The spanwise extent of each propeller slipstream is shown for clarity, and the clean-wing lift distribution is included as a reference. Results from both numerical models show the enhanced lifting performance resulting from the net increase in C_l within each propeller slipstream. The combined model over-predicts the increased lift in the upwash regions of the inboard and center propeller, although better agreement is attained for the outboard propeller. As discussed before, the overestimated profile within the slipstreams is likely caused by concentrating the hub, which is approximately 27% of the propeller radius in this setup, into a single point in the plane of the propeller. Additional discrepancy is observed between each slipstream, where the combined model under-predicts the local section lift. This is potentially caused by an overestimation of the negative axial velocity induced by vortex rings outside the slipstream. Accounting for these differences, the combined model estimates a wing lift coefficient of $C_L = 0.3901$, which is about 3.1% greater than the $C_L = 0.3783$ given by the CFD data.

Figure 3.24 shows the lift distributions for the counter-rotating configuration. Similar discrepancies from the co-rotating case are also seen here, but the change in the C_l gradient within the center propeller slipstream is effectively accounted for. General trends in the lifting behavior relative to the clean-wing configuration are predicted with reasonable accuracy. Between the inboard and center propellers, a combined downwash is induced, which reduces the section lift in this region compared to the clean-wing configuration. In contrast, a combined upwash is generated between the center and outboard propellers, which creates a notable net increase in the local lift. As before, the magnitudes of the C_l distribution between each slipstream are slightly underestimated. For this case, the combined model predicts $C_L = 0.3787$, which is 1.9% greater than the $C_L = 0.3718$ from the CFD data. Based on these outcomes, the combined model provides a good estimate of the enhanced lift for the distributed propulsion arrangement and will benefit from further improvements to better capture the details of the mutual interaction between the propellers.

3.4.4 Spanwise Induced Drag Distribution

Accurate modeling of the induced drag distribution is important for characterizing changes to the overall aerodynamic performance of a propeller-wing system. Compared to a clean wing, the combined system contains a modified induced drag component from the wing vortex lattice system due to local changes in the lattice circulation strengths caused by the propeller-induced loads. Additionally, a significant induced drag component is generated by the propeller swirl velocity. In this section, the spanwise induced drag behavior is compared with data from a parametric propeller-wing study by Nederlof et al. [36]. Their work utilized a blade element momentum model, a panel-based slipstream tube model with a correction for wake contraction, and the Weissinger method to analyze the collective effects of propeller-wing induced drag.

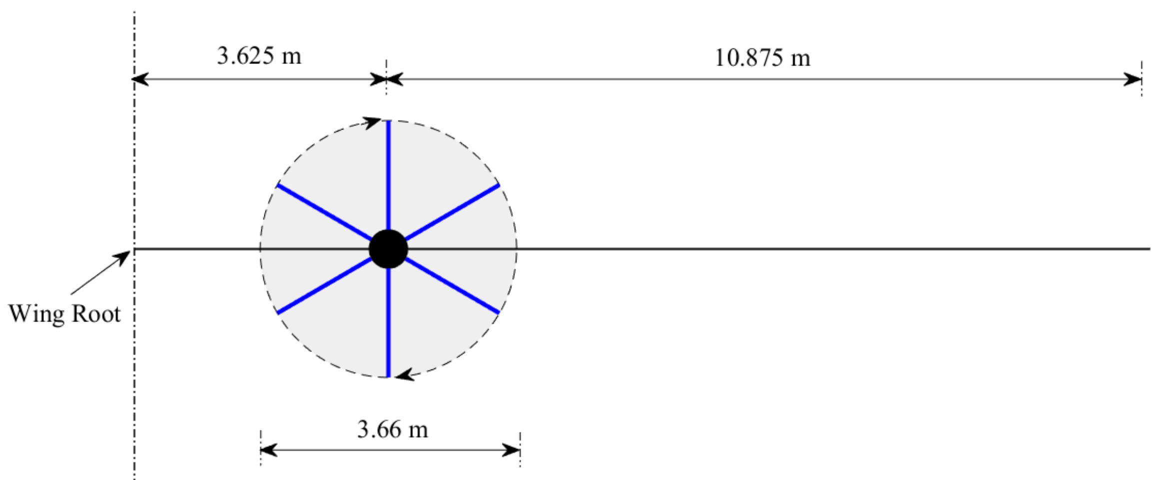

Figure 3.25: Propeller configuration based on the Fokker 50 with inboard-up rotation.

Comparisons of the induced drag distribution are made for two configurations, including one based on the Fokker 50 turboprop aircraft. In the first case, a six-bladed propeller with inboard-up rotation was positioned at $y/(b/2) = 0.25$, corresponding to the Fokker 50 design, but a simplified rectangular wing geometry was used. This setup is depicted in figure 3.25. For the second case, which is shown in figure 3.26, the propeller was moved to the wingtip. For each configuration, the propeller was located 2.13 m ahead of the wing

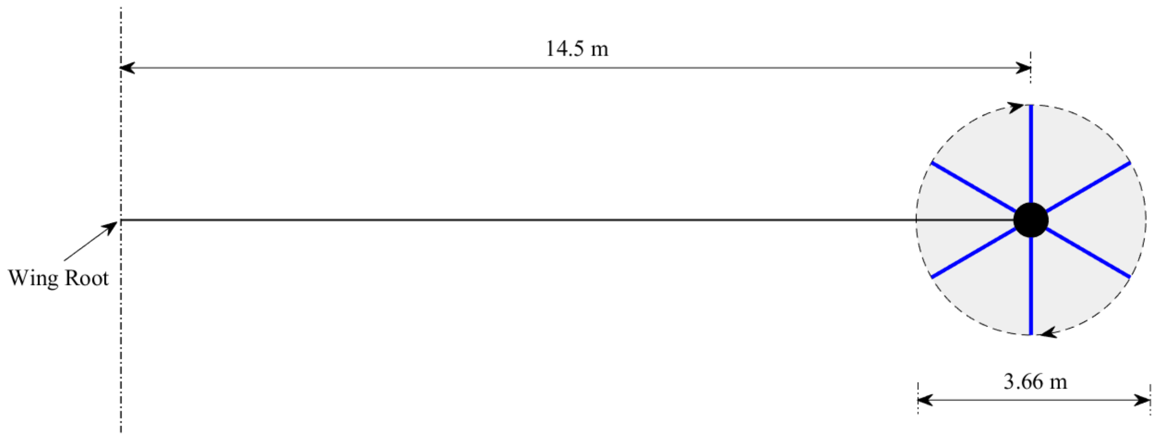

Figure 3.26: Wingtip propeller configuration with inboard-up rotation.

leading edge. Both cases were modeled for a typical cruise condition at an altitude of 7600 m, with a freestream air density of $\rho = 0.55$ kg/m^3, flight speed of $V_\infty = 140$ m/s and a combined system lift coefficient of $C_L = 0.35$.

The spanwise lift and induced drag distributions for the inboard propeller setup are presented in figures 3.27 and 3.28, respectively. Corresponding data for the clean wing is included for reference. Comparing both loading distributions, the combined model predictions show great agreement with the Nederlof data, which is likely due to the similarity of the methods used. For this case, both models show that changes to the induced drag distribution are largely confined to within the propeller slipstream. Over the inboard portion of the slipstream, the combined induced drag is largely reduced compared to the clean wing. This arises from the action of the propeller upwash, which tilts the lift vector of local wing panels in the direction opposite to the freestream, thereby generating a negative component of induced drag. The converse behavior is observed for the outboard side of the slipstream. Here, the propeller induces a downwash that generates additional induced drag along local wing panels. By inspection of figure 3.28, the combined effect within the slipstream integrates to a net negative induced drag that corresponds to a thrust force. Outside of the slipstream, the propeller upwash produces a small additional loading near the root. In order to retain the system lift coefficient at $C_L = 0.35$, the wing can therefore operate at a lower angle of attack. Further outboard, the induced drag variations for both the clean wing and combined

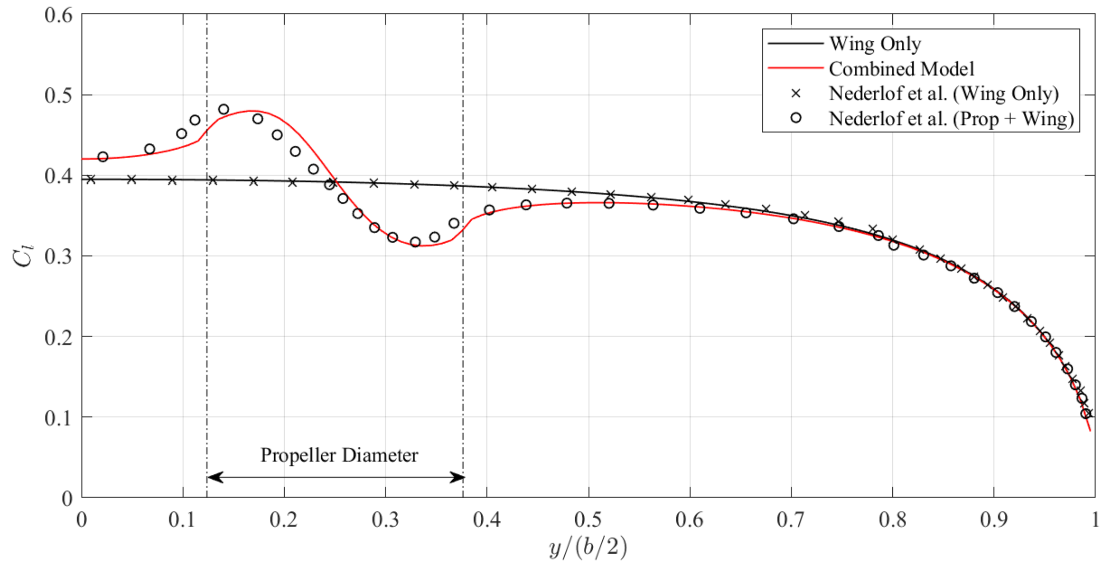

Figure 3.27: Spanwise lift distribution for a rectangular wing of $AR = 12$ with a propeller rotating inboard-up at $y/(b/2) = 0.25$; $b/2 = 14.5$ m, $c = 2.41$ m, $N_b = 6$, $R = 1.83$ m, $C_T = 0.23$, $J = 2.77$, $V_\infty = 140$ m/s, $C_L = 0.35$.

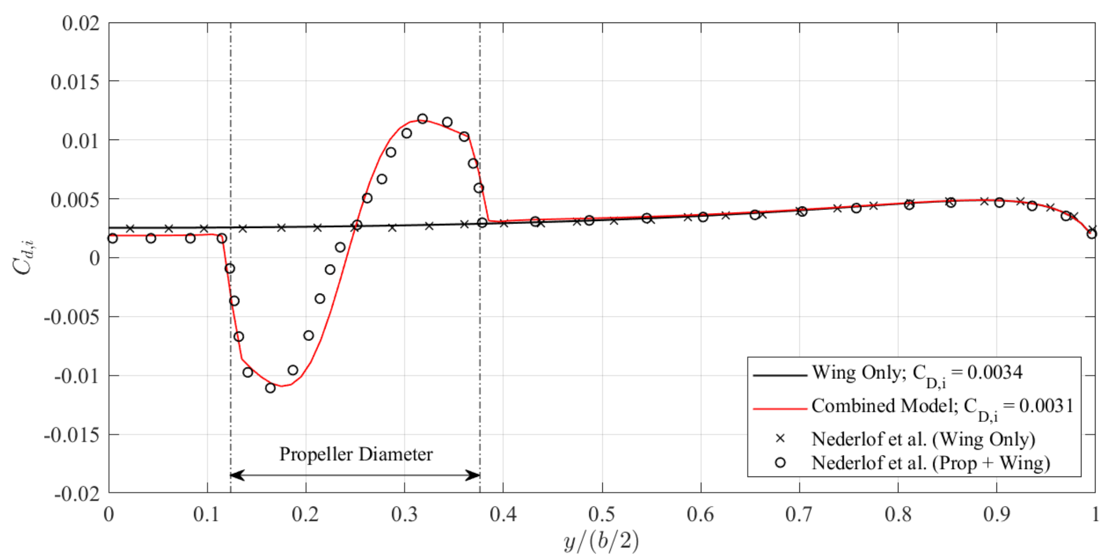

Figure 3.28: Spanwise induced drag distribution for a rectangular wing of $AR = 12$ with a propeller rotating inboard-up at $y/(b/2) = 0.25$; $b/2 = 14.5$ m, $c = 2.41$ m, $N_b = 6$, $R = 1.83$ m, $C_T = 0.23$, $J = 2.77$, $V_\infty = 140$ m/s, $C_L = 0.35$.

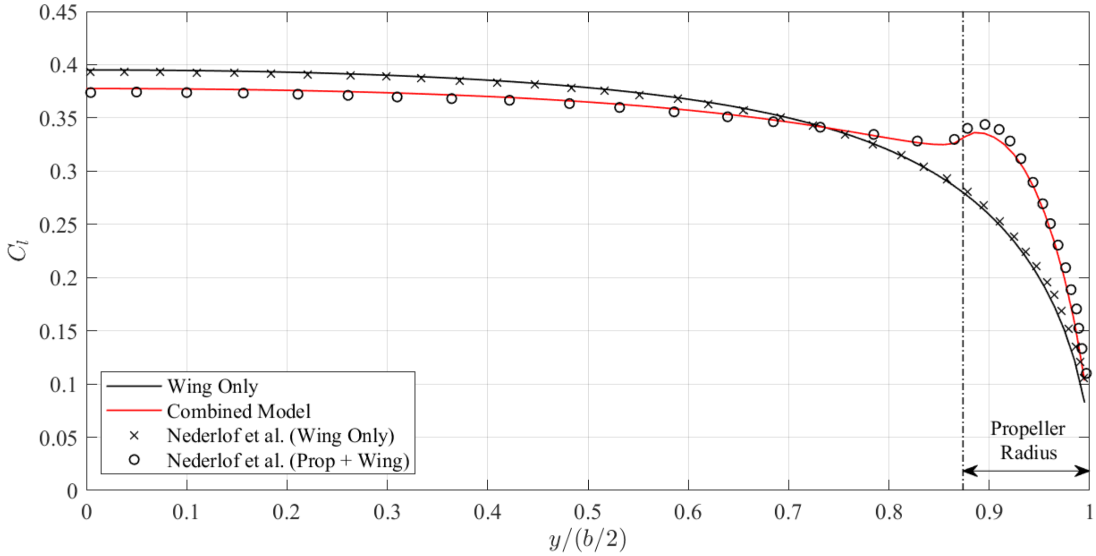

Figure 3.29: Spanwise lift distribution for a rectangular wing of $\text{Æ} = 12$ with a propeller rotating inboard-up at the wingtip; $b/2 = 14.5$ m, $c = 2.41$ m, $N_b = 6$, $R = 1.83$ m, $C_T = 0.23$, $J = 2.77$, $V_\infty = 140$ m/s, $C_L = 0.35$.

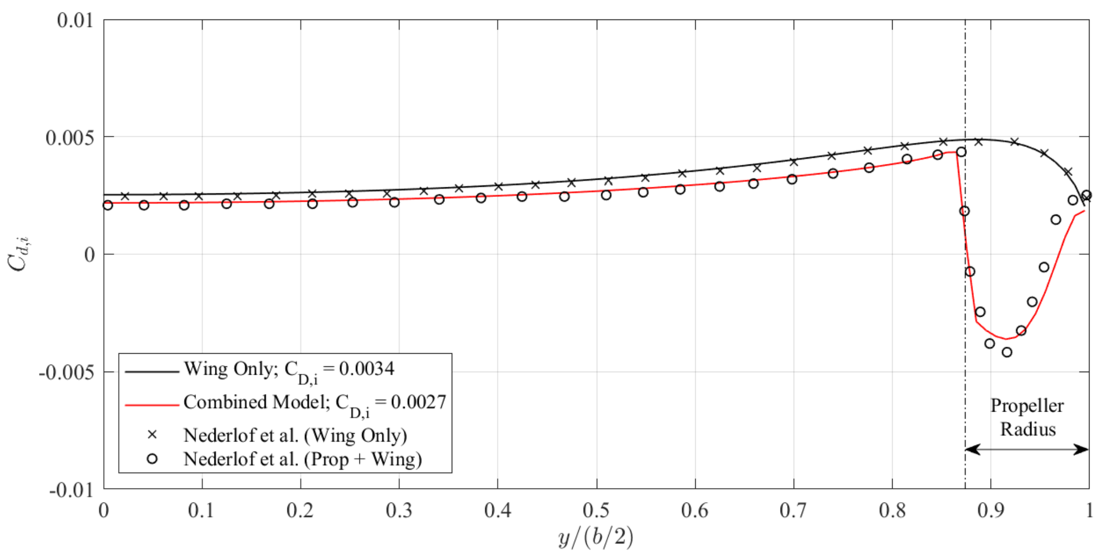

Figure 3.30: Spanwise induced drag distribution for a rectangular wing of $\text{Æ} = 12$ with a propeller rotating inboard-up at the wingtip; $b/2 = 14.5$ m, $c = 2.41$ m, $N_b = 6$, $R = 1.83$ m, $C_T = 0.23$, $J = 2.77$, $V_\infty = 140$ m/s, $C_L = 0.35$.

system are virtually the same due to the diminished slipstream effects near the wingtip.

Loading distributions for the second analysis case, where the propeller is positioned at the wingtip, are shown in figures 3.29 and 3.30. Again, the predicted distributions show excellent agreement with the numerical data from Neredlof et al. In this case, the upwash from the propeller generates additional lift for the portion of the wing immersed in the slipstream. This causes a notable decrease in the induced drag due to the forward tilting of local lift vectors for the immersed panels. Similar to the previous case, the added lift from the propeller upwash necessitates a reduction in the wing angle of attack to keep the system lift coefficient at $C_L = 0.35$. However, because the downwash region occurs beyond the wingtip, it does not contribute to a reduction in the overall C_L. Consequently, the wing can operate at a lower angle of attack than in the previous case. The overall reduction of induced drag along the wingspan demonstrates the greatly enhanced aerodynamic benefit of a tip-mounted propeller.

3.4.5 Total Induced Drag Coefficient

Nederlof et al. [36] also studied the effect of propeller spanwise position on total wing induced drag for the rectangular planform. Results from this study are compared with the combined model prediction in figure 3.31. For these comparisons, the induced drag coefficient is normalized by the corresponding value for a clean wing operating with the same total lift coefficient. Both models yield a similar variation in $C_{D,i}$ for different propeller locations along the half-span. At $y/(b/2) = 0.25$, corresponding to the Fokker 50 configuration, the combined model predicts an 11.3% decrease in the induced drag coefficient relative to the clean wing, compared to a 13.6% decrease predicted by Nederlof et al. As the propeller is moved further outboard, the total induced drag is gradually reduced from the net effects of the propeller swirl velocity. A greater reduction is observed as the propeller position surpasses about 85% of the half-span. This occurs because the downwash region of the slipstream begins to move increasingly beyond the wingtip, which mitigates the associated component of induced drag. For reference, the propeller radius, normalized by the half-span, is $R/(b/2) = 0.126$. It follows that outboard sections of the slipstream move off the wing

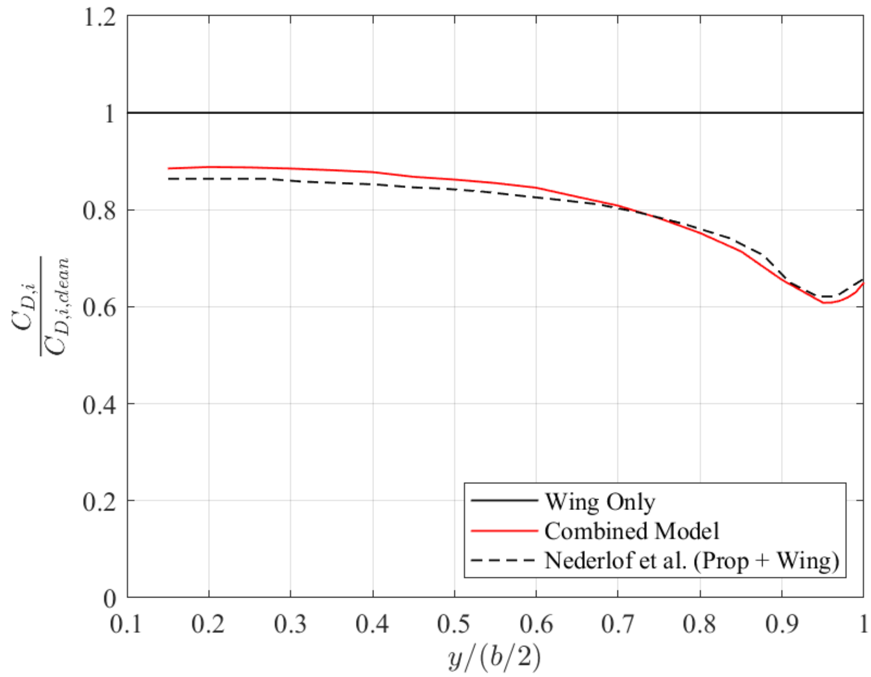

Figure 3.31: Variation of the total induced drag with propeller spanwise position for inboard-up rotation; $b/2 = 14.5$ m, $c = 2.41$ m, $N_b = 6$, $R = 1.83$ m, $C_T = 0.23$, $J = 2.77$, $V_\infty = 140$ m/s, $C_L = 0.35$.

when the propeller center is situated past $y/(b/2) = 0.874$. With the propeller at the wingtip, the combined model estimates a 35% reduction in the total induced drag, which is close to the 33.9% reduction estimated by Nederlof et al.

Both numerical models predict that the maximum induced drag reduction is attained when the propeller is located slightly inboard from the tip. A reason for this is that the magnitude of the propeller swirl velocity is small close to the propeller hub, so the downwash on the outboard side has little effect, even if a small part of that slipstream region aligns with the wing. By contrast, the upwash region more effectively reduces the induced drag slightly inboard, where the section lift is higher; this is due to the large negative spanwise loading gradient near the tip of a rectangular wing [36].

3.4.6 Lift-to-Induced Drag Ratio

The overall aerodynamic performance of the propeller-wing system studied by Nederlof et al. is evaluated through the lift-to-induced drag ratio. Figure 3.32 compares the variations of L/D_i with propeller spanwise position obtained from each model. As the propeller was moved towards the tip, the wing angle of attack was slightly reduced to keep the system lift coefficient at $C_L = 0.35$. The small discrepancies between the predictions are therefore largely a consequence of the total induced drag differences seen in figure 3.31. As a result, the combined model estimates a lower L/D_i increase over a large range of inboard propeller positions. Further outboard, however, it slightly overestimates the overall performance relative to the data from the validation study. These differences are likely caused by variations in the slipstream velocity modeling, particularly with the vortex core and wake contraction effects.

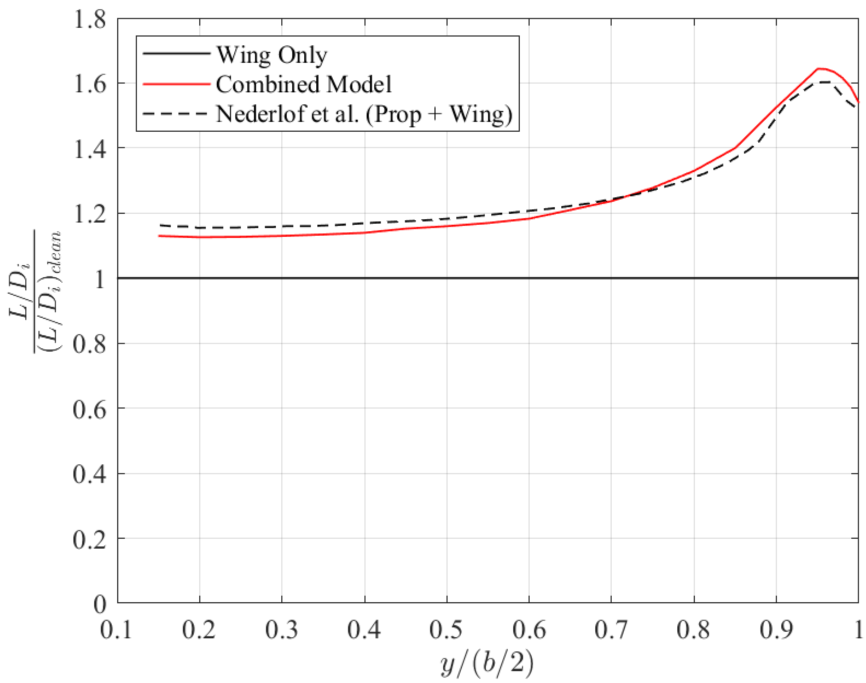

Figure 3.32: Variation of the total lift-to-induced drag ratio with propeller spanwise position for inboard-up rotation; $b/2 = 14.5$ m, $c = 2.41$ m, $N_b = 6$, $R = 1.83$ m, $C_T = 0.23$, $J = 2.77$, $V_\infty = 140$ m/s, $C_L = 0.35$.

In accordance with the observations from the previous section, the aerodynamic benefit of this system is maximized with the propeller positioned slightly inboard from the wingtip, around $y/(b/2) = 0.95$. At this location, the combined model estimates a peak L/D_i increase of about 64% over the clean wing, compared to a peak increase of 60% predicted by

Nederlof et al. Based on these comparisons, the developed model captures the aerodynamic performance quite effectively for this propeller-wing system.

Chapter 4

Conclusions

Ongoing research has demonstrated the potential benefits of distributed electric propulsion (DEP) in the aeronautical sector, including improved vehicle aerodynamics, enhanced takeoff performance, decreased fuel emissions, and reduced noise generation. As DEP technology continues to mature, a comprehensive understanding of the aerodynamics governing propeller-wing interaction is critical in order to optimize performance for various applications. Fast and accurate modeling of this interaction is especially important for preliminary design and analysis, serving as a primary objective of the present work.

In this thesis, a low-order propeller wake model was developed to efficiently calculate the time-averaged axial and tangential velocities in the slipstream. These calculations were combined with a Weissinger lifting-line method to analyze propeller-wing interactions, with a focus on capturing propeller-induced changes to the wing loading and overall aerodynamic performance. The combined model features several advantages over comparable methods due to its simplified nature. Since the propeller slipstream and wing are modeled separately, the propeller effects can be toggled on or off. This allows the aerodynamics of a combined propeller-wing system and a corresponding clean-wing configuration to be directly compared for more insightful analysis.

To reduce computational cost, the vortex wake model requires only basic information for the propeller geometry, including position, diameter and number of blades. It is therefore useful in analysis cases for which detailed blade section geometry is unavailable. The basic relationship between input variables also permits quick calculations of the vortex wake influence coefficients. As these can be readily scaled by the estimated circulation strengths, the slipstream induced velocities are computed without significant computational expense.

The assumptions made in the propeller wake model limit its scope of application, as outlined in section 2.4.1. Some aspects of the methods used result in the inability to accurately model certain conditions, such as static and highly-loaded propellers. However, within the applicable range, the developed model can still be applied to a broad set of cases. The validation studies demonstrate its ability to effectively handle a variety of conventional and distributed propulsion arrangements, as well as variations in spanwise propeller position and propeller rotation direction. Across the configurations analyzed, the model produces trends in the loading distributions and total wing loading that correlate generally well with higher-order methods and experimental data. The most significant discrepancies occur in part due to the propeller hub effects and related viscous effects, which are not completely accounted for. To address these matters, corrections could be made by including a separate mesh structure for the trailing hub vortex system to account for its dimensional extent, as well as incorporating a more robust viscous core model for the vortex rings to account for curvature.

Altogether, the current model serves as a feasible baseline for analyzing propeller-wing interactions. It provides a reasonable balance between efficiency and accuracy, while containing the flexibility to accommodate additional improvements in the future.

4.1 Future Work

Several aspects of the work in this thesis can be improved to enhance the combined model's accuracy and expand its capabilities. As previously noted, the additions of a dimensional hub vortex structure and a refined viscous core model could aid in mitigating the overestimation of aerodynamic effects produced by the propeller wake vortex system within the slipstream. This would lead to better predictions of the spanwise loading, which are especially important for assessing the localized effects of a propeller slipstream.

Small numerical discrepancies in the spanwise loading distributions may also be caused by misalignment of the propeller longitudinal vortices and the trailing vortices of the wing vortex lattice system. Currently, the trailing filaments corresponding to each vortex system are generated independently, so alignment is not guaranteed. An evident difficulty with aligning both trailing vortex systems in the current model is that the propeller longitudinal vortices are positioned using a uniform angular spacing around the slipstream circumference, which results in a non-uniform spacing along the spanwise direction. This could be corrected by implementing a variation of a cosine spacing method, which would necessitate further analysis to evaluate the subsequent effects on the tangential induced velocities in the slipstream.

A significant assumption of the combined model is that the propeller slipstream does not contract. Practically, this simplification is not too restrictive under certain conditions; however, it limits the accuracy of the model for highly-loaded propellers operating at low advance ratios, as discussed in section 2.4.1. This limitation may be accounted for by allowing the vortices of the propeller wake system to contract until the wake assumes an effectively constant diameter. With this approach, a more complex method would be required to determine the circulation strengths of the vortex elements in the contracting region of the wake. Additional calculations would also be needed to calculate the slipstream induced velocities due to the modified orientation of the vortex rings and rectilinear filaments. Alternatively, a prescribed wake contraction model could be utilized without significantly compromising the computational efficiency.

The developed model could also be extended to allow for small deformations of the wake due to propeller sideslip or incidence. In these cases, the bound vorticity is not distributed uniformly over the propeller disk, and the centerline of the vortex wake structure deviates slightly from the propeller axis. Thus, the influence coefficients for the propeller vortex elements would require reformulation. A possible solution to this problem involves treating the propeller wake influence as the sum of an axial component and a skew component, assuming perturbations to the wake geometry are small. By accommodating these changes, the model could be applied to a broader range of propeller configurations and operating conditions. This capability could also be leveraged to analyze rotors operating in vertical or forward flight.

The combined model may also benefit from further validation, particularly for evaluating the propeller influence on wings with various planform geometries. From comparisons with the rectangular planform studied by Nederlof et al. [36], it was determined that the net propeller slipstream effect on the wing is highly dependent on the shape of the clean-wing loading distribution, which in turn is a function of the wing planform geometry. This has notable implications for better understanding how propellers can be arranged along the wingspan in order to optimize overall aerodynamic performance.

Additional improvements can also be made to refine the computational performance of the current model. Although the methods used in this work allow for fast calculations of the propeller wake effects, certain aspects may benefit from a more efficient implementation. This is particularly important to ensure that any new capabilities added to the existing model have a minimal impact on the overall runtime.

REFERENCES

[1] Hyun D. Kim, Aaron T. Perry, and Phillip J. Ansell. A review of distributed electric propulsion concepts for air vehicle technology. In *AIAA/IEEE Electric Aircraft Technologies Symposium*, 2018.

[2] Jason A. Lechniak. LEAPTech/HEIST experiment test and evaluation summary. In *AIAA Aviation and Aeronautics Forum (Aviation 2018)*, Atlanta, GA, 2018.

[3] Arthur Dubois, Martin van der Geest, JoeBen Bevirt, Sean Clarke, Robert J. Christie, and Nicholas K. Borer. Design of an electric propulsion system for SCEPTOR. In *Aviation Technology, Integration, and Operations Conference*, Washington, D.C., 2016.

[4] Lukas Kiesewetter, Kazi Hassan Shakib, Paramvir Singh, Mizanur Rahman, Bhupendra Khandelwal, Sudarshan Kumar, and Krishna Shah. A holistic review of the current state of research on aircraft design concepts and consideration for advanced air mobility applications. *Progress in Aerospace Sciences*, 142:100949, 2023.

[5] Martin Schmuck, Juergen Garche, and Stefan Koller. Emerging aviation technologies - progress in the electrification of aircraft. In *8th European Conference for Aeronautics and Space Sciences EUCASS*, Madrid, 2019.

[6] W. J. M. Rankine. On the mechanical principles of the action of propellers. *Transactions of the Institution of Naval Architects*, 6, 1865.

[7] R. E. Froude. On the part played in propulsion by differences of fluid pressure. *Trans. Inst. Naval Architects*, 30:390, 1889.

[8] N. E. Joukowsky. Vortex theory of screw propeller, i. *Trudy Otdeleniya Fizicheskikh Nauk Obshchestva Lubitelei Estestvoznaniya*, 16(1):1–31, 1912.

[9] L. Prandtl. Tragflügeltheorie. i. mitteilung. *Nachrichten von der Gesellschaft der Wissenschaften zu Göttingen, Mathematisch-Physikalische Klasse*, 1918:451–477, 1918.

[10] J. Weissinger. The lift distribution of swept-back wings. Technical Report 1120, National Advisory Committee for Aeronautics, Washington, D.C., March 1947.

[11] Sandi Kawada. Induced velocity by helical vortices. *Journal of the Aeronautical Sciences*, 3(3):86–87, 1936.

[12] Jay C. Hardin. The velocity field induced by a helical vortex filament. *The Physics of Fluids*, 25(11):1949–1952, 11 1982.

[13] Y. Fukumoto and V. L. Okulov. The velocity field induced by a helical vortex tube. *Physics of Fluids*, 17(10):107101, 10 2005.

[14] Sandeep Gupta and J. Gordon Leishman. Accuracy of the induced velocity from helicoidal wake vortices using straight-line segmentation. *AIAA Journal*, 43(1):29–40, 2005.

[15] Ryan J. Welker. Low-order modeling of propeller vortex-wing interaction using discretized helical filaments and Weissinger method. Master's thesis, North Carolina State University, Raleigh, North Carolina, 2023.

[16] Valery L. Okulov, Jens N. Sørensen, and David H. Wood. The rotor theories by professor Joukowsky: Vortex theories. *Progress in Aerospace Sciences*, 73:19–46, 2015.

[17] R. I. Lewis. *Bodies of revolution, ducts and annuli*, page 146–190. Cambridge Engine Technology Series. Cambridge University Press, 1991.

[18] J W van Heemst, D Baldacchino, D Mehta, and G J W van Bussel. Coupling of a free wake vortex ring near-wake model with the Jensen and Larsen far-wake deficit models. *Journal of Physics: Conference Series*, 625(1):012041, June 2015.

[19] Issam Meghlaoui, Ivan Dobrev, Fawaz Massouh, Abdelouahab Benretem, and Dalila Khalfa. Accelerated computation of the wake of a horizontal axis wind turbine in unsteady operation using the vortex approach. *Applied Journal of Environmental Engineering Science*, 5(1):al–Appl, 2019.

[20] Rodolfo Bontempo and Marcello Manna. A ring-vortex free-wake model for uniformly loaded propellers. Part 1-model description. *Energy Procedia*, 148:360–367, 2018. ATI 2018 - 73rd Conference of the Italian Thermal Machines Engineering Association.

[21] Rodolfo Bontempo and Marcello Manna. Verification of the axial momentum theory for propellers with a uniform load distribution. *International Journal of Turbomachinery, Propulsion and Power*, 4(2):8, 2019.

[22] Emmanuel Branlard and Mac Gaunaa. Cylindrical vortex wake model: right cylinder. *Wind Energy*, 18(11):1973–1987, 2015.

[23] B. W. McCormick. *Aerodynamics of V/STOL Flight*. Academic Press, New York, 1967.

[24] John T. Conway. Analytical solutions for the actuator disk with variable radial distribution of load. *Journal of Fluid Mechanics*, 297:327–355, 1995.

[25] Kunio Kuwahara and Hideo Takami. Numerical studies of two-dimensional vortex motion by a system of point vortices. *Journal of the Physical Society of Japan*, 34(1):247–253, 1973.

[26] J. L. Hess and A.M.O. Smith. Calculation of potential flow about arbitrary bodies. *Progress in Aerospace Sciences*, 8:1–138, 1967.

[27] Dong-Geun Baek, Hyun-Sik Yoon, Jae-Hwan Jung, Ki-Sup Kim, and Bu-Geun Paik. Effects of the advance ratio on the evolution of a propeller wake. *Computers & Fluids*, 118:32–43, 2015.

[28] Franklin W Diederich and Martin Zlotnick. Calculated spanwise lift distributions and aerodynamic influence coefficients for swept wings in subsonic flow. Technical report, National Advisory Committee for Aeronautics, 1955.

[29] J. Lepicovsky and W. A. Bell. Aerodynamic measurements about a rotating propeller with a laser velocimeter. *Journal of Aircraft*, 21(4):264–271, 1984.

[30] Douglas Hunsaker and Deryl Snyder. A lifting-line approach to estimating propeller/wing interactions. In *24th AIAA Applied Aerodynamics Conference*, page 3466, 2006.

[31] J Stuper. Effect of propeller slipstream on wing and tail. Technical report, National Advisory Committee for Aeronautics, 1938.

[32] Youngrock Seo, Yoonpyo Hong, and Kwanjung Yee. Numerical investigation of wing–multiple propeller aerodynamic interaction using actuator disk method. *International Journal of Aeronautical and Space Sciences*, 23(5):805–822, 2022.

[33] LLM Veldhuis. Analysis of propeller slipstream effects on a trailing wing. In *ICAS PROCEEDINGS*, volume 20, pages 2392–2413, 1996.

[34] Lynn W Hunton. Effects of finite span on the section characteristics of two 45° swept-back wings of aspect ratio 6. *NACA TN*, 3008, 1953.

[35] LLM Veldhuis. Review of propeller-wing aerodynamic interference. In *24th International Congress of the Aeronautical Sciences*, volume 6, pages 2004–6. Optimage Ltd. Edinburgh, UK, 2004.

[36] Robert Nederlof, Robert Kooij, Leo L Veldhuis, and Tomas Sinnige. Contribution of swirl recovery to the induced drag of a propeller-wing system–a parametric study. In *AIAA AVIATION 2023 Forum*, page 3543, 2023.